Global Biogeochemical Cycles

RESEARCH ARTICLE
10.1029/2025GB008713

Key Points:

- Ocean biogeochemical models contain systematic seasonal biases that impact the evolution of surface ocean pCO_2 seasonality
- Differing model sensitivities to anthropogenic carbon cause a divergence in model pCO_2 seasonal cycle amplitude changes over time
- Diverging model representations of pCO_2 seasonality change lead to diverging model estimates of the net annual sea-air CO_2 flux

Supporting Information:

Supporting Information may be found in the online version of this article.

Correspondence to:
M. C. Arroyo,
mar.arroyo@noaa.gov

Citation:
Arroyo, M. C., Fassbender, A. J., & Rodgers, K. B. (2026). The increasing impact of seasonality biases on model-based estimates of the ocean carbon sink. *Global Biogeochemical Cycles*, *40*, e2025GB008713. https://doi.org/10.1029/2025GB008713

Received 11 JUN 2025
Accepted 9 FEB 2026

The Increasing Impact of Seasonality Biases on Model-Based Estimates of the Ocean Carbon Sink

Mar C. Arroyo[1,2], **Andrea J. Fassbender**[1,2], **and Keith B. Rodgers**[3,4]

[1]Department of Ocean Sciences, University of California Santa Cruz, Santa Cruz, CA, USA, [2]NOAA/OAR Pacific Marine Environmental Laboratory, Seattle, WA, USA, [3]Advanced Institute for Marine Ecosystem Change (WPI-AIMEC), Tohoku University, Sendai, Japan, [4]WPI-AIMEC, Japan Agency for Marine-Earth Science and Technology (JAMSTEC), Yokohama, Japan

Abstract Ocean carbon cycle syntheses combine observation-based surface ocean pCO_2 products and global ocean biogeochemical models (GOBMs) to estimate air-sea CO_2 fluxes. These efforts show that GOBMs underestimate the ocean's anthropogenic CO_2 sink compared to observation-based products, though the causes remain uncertain. Observations and models indicate that the seasonal amplitude of surface pCO_2 is increasing due to anthropogenic carbon (C_{ant}) accumulation, potentially altering net annual CO_2 fluxes. Here, we test the hypothesis that systematic biases in model representations of surface pCO_2 seasonality contribute to long-term biases in annual ocean carbon uptake trends. Using simulations from seven GOBMs, we evaluate changes in surface pCO_2 seasonal amplitude over 1980–2018, separating contributions from C_{ant} accumulation and climate-state changes. Within each model, seasonal pCO_2 amplitude growth is primarily caused by C_{ant}-driven enhancement in pCO_2 sensitivity to seasonal thermal and biophysical processes. Across models, differences in C_{ant}-driven pCO_2 amplification are closely linked to differences in initial seasonal variability of surface temperature and dissolved inorganic carbon. Models with larger seasonal pCO_2 amplitudes in 1980–1984 exhibit proportionally larger C_{ant}-driven growth, widening the across-model disagreement in seasonal pCO_2 amplitudes over time. Consequently, growing model disagreement in wintertime sea-air pCO_2 disequilibrium causes divergence in cumulative ocean carbon sink estimates. Seasonal wind variability may further modulate CO_2 flux differences, but its role could not be directly assessed. These findings demonstrate that systematic seasonal pCO_2 biases contribute to diverging annual ocean carbon uptake trends, highlighting the importance of improving seasonal carbon cycle process representations to reduce uncertainty in future climate change projections.

1. Introduction

The ocean is a major sink for anthropogenic carbon dioxide (CO_2) emissions (Friedlingstein et al., 2024), serving as a key regulator of Earth's climate. The flux of anthropogenic carbon (C_{ant}) into the surface ocean increases the inventory of dissolved inorganic carbon (DIC) (DeVries et al., 2023; Gruber et al., 2019; Khatiwala et al., 2013; Müller et al., 2023) and causes shifts in seawater carbonate chemistry (Broecker et al., 1979; Middelburg et al., 2020; Revelle & Suess, 1957; Rodgers et al., 2020; Toyama et al., 2017). C_{ant} accumulation increases the partial pressure of CO_2 (pCO_2) and diminishes carbonate ion concentrations, leading to the progressive erosion of the ocean's buffer capacity and reduction in CO_2 uptake efficiency. These secular alterations in mean-state ocean conditions on annual to multi-annual timescales represent a positive feedback on Earth's changing climate, with a weakening ocean carbon sink leading to a larger remaining fraction of emitted CO_2 gas in the atmosphere over time (Muller et al., 2023; Rodgers et al., 2020). It is therefore critical to understand how the ocean carbon cycle responds to rising atmospheric CO_2 to better constrain the changing ocean carbon sink.

Synthesis efforts to track the historical evolution of the ocean carbon sink, including the Global Carbon Project (Friedlingstein et al., 2024) and the recent REgional Carbon Cycle Assessment and Processes Phase 2 (RECCAP2) initiative (DeVries et al., 2023; Terhaar et al., 2024), use air-sea CO_2 flux estimates from global ocean biogeochemical models (GOBMs; Hauck et al., 2020) and observation-based pCO_2 data products (Rödenbeck et al., 2015). GOBMs are hindcast models forced by reanalysis data that simulate physical and biogeochemical processes influencing the ocean carbon cycle under transient atmospheric CO_2 and climate variability. Because these models represent both natural and anthropogenic carbon fluxes, they are implicitly used in the Global Carbon Budget to quantify anthropogenic perturbations of the ocean carbon sink. These models, however, are

© 2026. The Author(s).
This is an open access article under the terms of the Creative Commons Attribution License, which permits use, distribution and reproduction in any medium, provided the original work is properly cited.

known to contain systematic biases that contribute to uncertainties in air-sea CO_2 flux estimates (DeVries et al., 2023; Fay & McKinley, 2021; Khatiwala et al., 2013; Terhaar et al., 2024; Wanninkhof et al., 2013). Notably, GOBMs generally underestimate the globally integrated ocean carbon sink strength relative to data-product-based estimates (Friedlingstein et al., 2024) and exhibit substantial inter-model differences in CO_2 flux variability (Hauck et al., 2020; Terhaar et al., 2024). Discrepancies in GOBM-based CO_2 fluxes partly reflect biases in the mean-state surface ocean carbonate chemistry, which dictates the buffer capacity for C_{ant} uptake, and in ocean circulation, which controls C_{ant} transport from the surface into the interior ocean (Terhaar et al., 2024). Inter-model differences in air-sea CO_2 fluxes are also tightly linked to structural differences in pre-industrial spin-up procedures (Terhaar et al., 2024), as standardization remains difficult given the differing model complexities and substantial computational cost (e.g., Séférian, Delire, et al., 2016; Séférian, Gehlen, et al., 2016). Additional sources of model-product discrepancy come from biases in the observation-based pCO_2 data products themselves due to the spatiotemporal sparsity in data sampling and inherent uncertainties in statistical or machine-learning gap filling methodologies (Bushinsky et al., 2019; Gloege et al., 2021; Gregor et al., 2019; Hauck et al., 2023; Mayot et al., 2024).

GOBMs simulate the seasonal variability of air-sea CO_2 fluxes, which allows us to assess how seasonal carbon cycle representations influence model-based estimates of the ocean carbon sink (Rodgers et al., 2023). Because surface pCO_2 variations strongly regulate air-sea CO_2 fluxes, changes in the amplitude, structure, or phase of pCO_2 seasonality may alter the cumulative annual ocean carbon sink (Fassbender et al., 2018, 2022; Gorgues et al., 2010; Hauck & Völker, 2015; Kessler & Tjiputra, 2016; Nevison et al., 2016; Riebesell et al., 2009; Rodgers et al., 2008). Across much of the open ocean, the amplitude of surface pCO_2 seasonal cycles is increasing primarily due to C_{ant}, as recorded by observations (Landschützer et al., 2018) and GOBM reconstructions (Rodgers et al., 2023). This amplification occurs because C_{ant} accumulation enhances the sensitivity of pCO_2 (i.e., its response) to natural seasonal processes through associated declines in buffer capacity (Fassbender et al., 2018; Gallego et al., 2018; Hauck & Völker, 2015; Kwiatkowski & Orr, 2018; Riebesell et al., 2009). Using one large-ensemble Earth System Model (ESM), Fassbender et al. (2022) found that accounting for the C_{ant}-driven amplification in pCO_2 seasonality leads to a modest increase in the global ocean carbon sink (by ~8%) over the 21st century. The influence of wintertime surface pCO_2 changes is enhanced by stronger winter winds, giving greater efficacy to the wintertime CO_2 sink season. Thus, C_{ant}-induced seasonal pCO_2 changes may act as a negative feedback on changes in the Earth's climate, enhancing ocean carbon uptake and partially offsetting the larger, positive annual mean-state feedback that weakens the ocean carbon sink (e.g., Rodgers et al., 2020).

Motivated by the link between pCO_2 seasonal cycle alterations and changing ocean carbon uptake, this study investigates historical changes in surface pCO_2 seasonal cycle amplitudes in multiple GOBMs used for carbon budgeting. Previous studies using GOBMs (Fay & McKinley, 2021; Hauck et al., 2020; Rodgers et al., 2023) and structurally similar ESMs (Goris et al., 2018; Kessler & Tjiputra, 2016; Mongwe et al., 2018; Nevison et al., 2016; Rustogi et al., 2023) have identified systematic biases in seasonal pCO_2 variations, particularly in northern subpolar regions and the Southern Ocean. How these seasonal biases evolve under C_{ant}-driven changes to annual mean-state conditions to influence ocean carbon sink estimates remains understudied across multiple GOBMs. Although mean-state frameworks often assume that timescales of variability are independent and thus linear, changes in the seasonal pCO_2 cycle may influence annual pCO_2 trends through rectification, as seasonal anomalies modulate net air-sea CO_2 fluxes through nonlinear carbonate system responses (Fassbender et al., 2018, 2022). Here, we test the hypothesis that across-model differences in annual ocean carbon uptake trends stem in part from biases in their seasonal cycle representations. Building on Rodgers et al. (2023), we evaluate and compare the simulated changes in pCO_2 seasonal cycle amplitudes from 1980 to 2018 across multiple GOBMs, isolating the impacts of C_{ant} accumulation and changing physical climate. We aim to demonstrate how systematic biases in seasonal carbon cycle drivers influence the seasonal pCO_2 amplitude change and the cumulative annual ocean carbon sink strength over time.

2. Methods

2.1. Global Ocean Biogeochemical Models

We used simulations from a subset of GOBMs provided by the ocean section of RECCAP2 (Müller, 2023) to evaluate the changes in surface ocean pCO_2 seasonal cycles between 1980 and 2018 (Table 1). GOBM output is provided as monthly means at 1° × 1° horizontal resolution. All models were forced with historical levels of

Table 1
Global Ocean Biogeochemical Models and Their Physical Climate Forcing Products Used in This Study

Model	Reference	Physical climate forcing	Notes
CCSM-WHOI (CCSM 3.1)	Doney et al. (2009)	CORE and NCEP/NCAR	Ends in 2017
CESM-ETHZ	Lindsay et al. (2014); Yang and Gruber (2016)	CORE and JRA-55	
CNRM-ESM-1	Berthet et al. (2019); Séférian, Delire, et al., 2016; Séférian et al. (2019)	JRA-55	
EC-Earth3	Aumont et al. (2015); Döscher et al. (2022)	JRA-55	
FESOM-REcoM-LR	Hauck et al. (2020)	JRA-55	No preindustrial spin-up; Used WOA18 phosphate
NorESM-OC1.2	Schwinger et al. (2016)	CORE	
ORCA025-GEOMAR	Chien et al. (2022); Kriest and Oschlies (2015)	JRA-55	No preindustrial spin-up; Used WOA18 silicate

Note. WOA18 = World Ocean Atlas 2018.

atmospheric CO_2 and observational-based reanalysis of physical climate products (e.g., wind, temperature, precipitation, and humidity) to resolve the source, sink, and transport processes of the ocean carbon cycle. For all simulations, most models first performed a pseudo-preindustrial spin-up procedure, forced with a constant atmospheric CO_2 fixed at pre-industrial levels and a repeated normal-year (climatological) physical climate forcing (Table 1; see DeVries et al., 2023 Supporting Information). The goal of this initial spin-up phase is for the models to reach a steady state where air-sea CO_2 fluxes become time-invariant on multi-year timescales and globally sum to zero before industrialization. After industrialization, models continue to use normal-year physical forcing until transient historical reanalysis forcing fields become available. Incomplete spin-ups, in which a model has not fully reached a steady state with respect to carbon fluxes at industrialization, introduce biases (constant in time) and drifts (time evolving) that differ between models, and are retained through the simulations (Hauck et al., 2020). Physical forcing products used by these GOBMs include CORE (Large & Yeager, 2009), JRA-55 (Kobayashi et al., 2015), and NCEP/NCAR (Kalnay et al., 1996; Table 1). Additionally, only some models simulate carbon transport from land by rivers or carbon burial in sediments. Detailed information about model performance and comparisons of carbon cycle processes against observation-based data products can be found in recent RECCAP2 chapters (DeVries et al., 2023; Rodgers et al., 2023; Terhaar et al., 2024). For our analysis, we excluded sea ice-covered regions in the Arctic Ocean and high-latitude Southern Ocean due to the paucity of seasonal pCO_2 observations available to validate model performance.

2.2. Quantifying Mechanisms of Surface Ocean pCO_2 Seasonal Cycle Amplitude Change

Each GOBM performed four historical simulations, allowing us to independently quantify the effects of increasing atmospheric CO_2 and changes in physical climate state on the reconstructed surface ocean pCO_2 seasonal cycle amplitudes (Table 2). For each model, seasonal cycle amplitudes of pCO_2 (A-pCO_2) are computed as the local maximum minus minimum value in each simulation year (Figure 1a). Since we are interested in multi-decadal changes, the change in pCO_2 seasonal cycle amplitude (ΔA-pCO_2) is computed by subtracting the mean A-pCO_2 between 1980 and 1984 from the mean A-pCO_2 between 2014 and 2018 (e.g., ΔA-pCO_2 = A-$pCO_2^{2014-2018}$ – A-$pCO_2^{1980-1984}$). Seasonal cycle amplitudes are averaged over the 5-year periods to smooth for interannual variability before computing the amplitude change, similar to prior methodologies (Landschutzer et al., 2018; Rodgers et al., 2023). Output from the CCSM-WHOI model (Doney et al., 2009; Table 1) is only available through 2017, so we consider climatology and averages over 2014–2017 for this model.

Simulation A (Sim *A*) is a contemporary simulation using transient rising atmospheric CO_2 and time-evolving physical forcing, capturing the net effect of anthropogenic and natural carbon cycle processes. The total change in A-pCO_2 (Δ_{total} A-pCO_2) is evaluated over this simulation as the combined impact of C_{ant} accumulation and changes in physical climate due to both internal climate variability and anthropogenic climate change. This term also includes the non-steady-state changes in A-pCO_2 associated with the interaction between rising atmospheric CO_2 and changing physical climate.

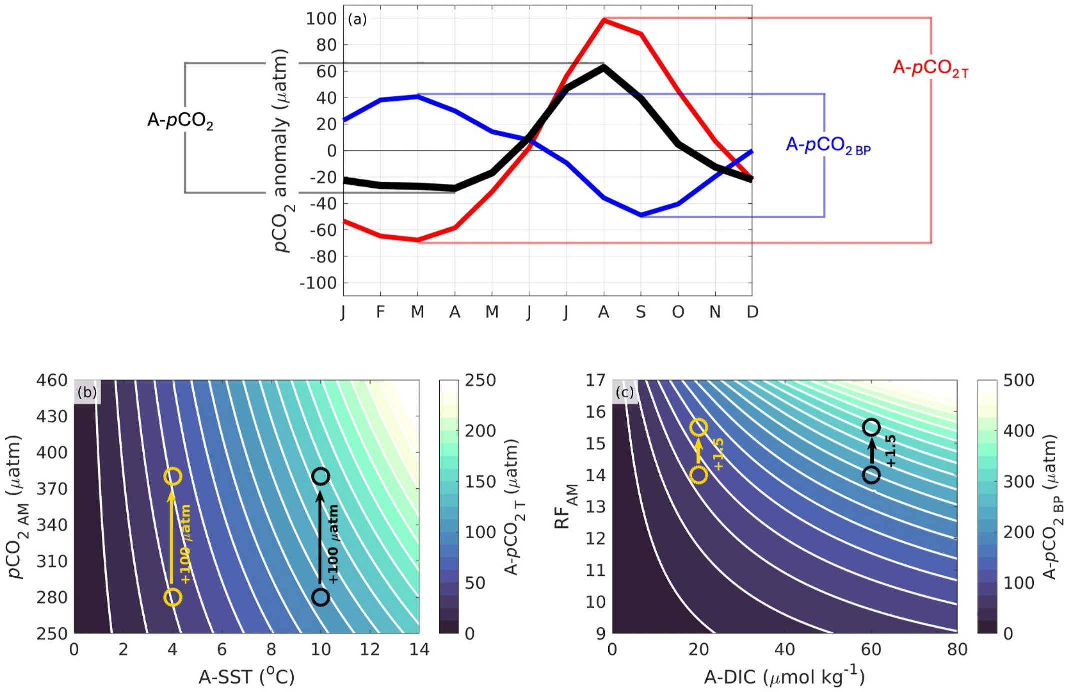

Figure 1. (a) An example decomposition of $p\text{CO}_2$ seasonal cycle amplitudes (A-$p\text{CO}_2$, black) into thermal (A-$p\text{CO}_{2\ \text{T}}$, red) and biophysical (A-$p\text{CO}_{2\ \text{BP}}$, blue) components in a thermally dominated subtropical region in the Northern Hemisphere. Seasonal cycle amplitudes are computed as the local maximum value minus the local minimum value each year. (b) A-$p\text{CO}_{2\ \text{T}}$ as a function of sea surface temperature seasonal cycle amplitude (A-SST) and annual mean $p\text{CO}_2$ ($p\text{CO}_{2\ \text{AM}}$), and (c) A-$p\text{CO}_{2\ \text{BP}}$ as a function of dissolved inorganic carbon seasonal cycle amplitude (A-DIC) and annual mean Revelle Factor (RF_{AM}). Yellow and black annotations represent theoretical changes in sensitivity factors ($p\text{CO}_{2\ \text{AM}}$ and RF_{AM}) at different initial variability driver (A-SST and A-DIC) conditions (see text). Contours were generated using CO2SYS with total alkalinity = 2350 μmol/kg, temperature = 18°C, salinity = 34.8, silicate = 15 μmol/kg, and phosphate = 1.5 μmol/kg.

Table 2
Derived Quantities and Their Definitions

Symbol	Definition	Equation	Description
Δ_{total} A-X	Total change in seasonal cycle amplitude of variable X	Equation 1	Accounts for the combined impact of C_{ant} accumulation and changes in physical climate due to internal climate variability and climate change
$\Delta_{\text{Cant-SS}}$ A-X	Change in seasonal cycle amplitude of variable X caused by steady-state C_{ant} accumulation	Equation 2	Accounts for the impact of steady-state C_{ant} accumulation under repeated physical climate variability (i.e., no climate change)
Δ_{Cant} A-X	Change in seasonal cycle amplitude of variable X caused by total C_{ant} accumulation	Equation 4	Accounts for the combined impact of steady-state C_{ant} accumulation and the non-steady-state changes due to interactions between C_{ant} and changes in physical climate
Δ_{clim} A-X	Change in seasonal cycle amplitude of variable X caused by changes in the physical climate state	Equation 3	Accounts for the impact of changes in physical climate due to internal climate variability and climate change

Note. Seasonal cycle amplitudes (A) for each variable (X) are computed as the local maximum minus minimum value in each simulation year. Multi-decadal changes in seasonal amplitudes for each variable are computed between the 1980–1984 and 2014–2018 mean periods. Variables include $p\text{CO}_2$, $p\text{CO}_{2\ \text{T}}$, $p\text{CO}_{2\ \text{BP}}$, SST, and DIC.

$$\Delta_{\text{total}}\ \text{A-}p\text{CO}_2 = \text{Sim}\ A\ \text{A-}p\text{CO}_2^{2014-2018} - \text{Sim}\ A\ \text{A-}p\text{CO}_2^{1980-1984} \tag{1}$$

Simulation B serves as a control run, forced with constant pre-industrial atmospheric CO_2 levels and repeated normal-year physical forcing. We use *Simulation B* to estimate the models' drift over time. Because drifts in pCO_2 seasonal cycle amplitude are extremely small between 1980 and 2018 in each model (Figure S1 in Supporting Information S1), we do not correct for model drift as many RECCAP2 studies do.

In *Simulation C* (Sim *C*), atmospheric CO_2 levels increase at historical rates, while the physical climate remains constant under repeated normal-year forcing. This simulation is used to isolate the steady-state impact of C_{ant} accumulation on seasonal pCO_2 amplitudes ($\Delta_{\text{Cant-SS}}$ A-pCO_2) in the absence of changes in the climate state.

$$\Delta_{\text{Cant-SS}}\ \text{A-}p\text{CO}_2 = \text{Sim}\ C\ \text{A-}p\text{CO}_2^{2014-2018} - \text{Sim}\ C\ \text{A-}p\text{CO}_2^{1980-1984} \tag{2}$$

Lastly, *Simulation D* (Sim *D*) is forced with constant pre-industrial atmospheric CO_2 and time-evolving physical forcing (i.e., with radiative warming). We use this simulation to isolate the impact of changes in the physical climate on seasonal pCO_2 amplitudes (Δ_{clim} A-pCO_2) due to both internal climate variability and climate change.

$$\Delta_{\text{clim}}\ \text{A-}p\text{CO}_2 = \text{Sim}\ D\ \text{A-}p\text{CO}_2^{2014-2018} - \text{Sim}\ D\ \text{A-}p\text{CO}_2^{1980-1984} \tag{3}$$

In the real world, changes in the physical climate state further modify C_{ant} concentrations in the upper ocean by altering CO_2 gas solubility, water column density structure, and/or biological processes. Because *Simulation C* does not capture this nonlinear, non-steady-state contribution to the C_{ant} pool, we estimate the total C_{ant} perturbation on seasonal pCO_2 amplitude changes (Δ_{Cant} A-pCO_2) by subtracting *Simulation D* from *Simulation A* over the two time periods. This term accounts for both steady-state and non-steady-state accumulations of C_{ant}.

$$\Delta_{\text{Cant}}\ \text{A-}p\text{CO}_2 = (\text{Sim}\ A - \text{Sim}\ D)\ \text{A-}p\text{CO}_2^{2014-2018} - (\text{Sim}\ A - \text{Sim}\ D)\ \text{A-}p\text{CO}_2^{1980-1984} \tag{4}$$

A summary of the derived quantities used throughout the paper can be found in Table 2. Our approach to quantify changes in A-pCO_2 and its drivers by subtracting the initial 1980–1984 period from the ending 2014–2018 period removes model biases and drifts (until 1980) as well as steady-state fluxes prior to industrialization. Further, we do not correct for models that simulate riverine carbon exchange or carbon burial processes, as we assume these processes do not substantially influence open-ocean pCO_2 seasonal cycles and their anthropogenic changes on these timescales.

2.3. Thermal and Biophysical Drivers of pCO_2 Seasonality and Carbonate System Calculations

Surface ocean pCO_2 seasonality is controlled by regionally varying and often competing thermal, physical, and biogeochemical processes. To mechanistically understand how C_{ant} accumulation and changes in physical climate influence these drivers to alter pCO_2 seasonal cycle amplitudes, we employ the methodology of Fassbender et al. (2022) to decompose simulated pCO_2 seasonal cycles into thermal (T) and biological and physical (biophysical; BP) components in each model. The pCO_2 decomposition method by Fassbender et al. (2022) was originally applied to ESM output and builds upon the empirical framework initially put forth by Takahashi et al. (1993, 2002). This methodology preserves asymmetric seasonal pCO_2 changes that may alter the phasing of the seasonal pCO_2 cycle.

Within the framework of Fassbender et al. (2022), it is first necessary to define a neutral state about which seasonal variations can be identified. For each model, simulation year, and grid cell, we first compute the annual mean (AM) pCO_2 using the annual means of its drivers: sea surface temperature (SST), sea surface salinity (SSS), DIC, total alkalinity (TA), and inorganic nutrients (phosphate, PO_4; silicate, Si).

$$p\text{CO}_{2\ \text{AM}} = f\left(\overline{\text{SST}}, \overline{\text{SSS}}, \overline{\text{DIC}}, \overline{\text{TA}}, \overline{\text{PO}_4}, \overline{\text{Si}}\right) \tag{5}$$

Here, *f* signifies a carbonate system calculator, and overbars denote annual mean values. Climatological estimates of seasonal sea surface PO_4 and Si values were obtained from the World Ocean Atlas 2018 for models that did not provide those output fields (Table 1). Computing the annual mean pCO_2 from its drivers rather than an average of monthly $p\text{CO}_2$ values produces a value that is less influenced by seasonal $p\text{CO}_2$ extrema and thermodynamically consistent with the annual means of its drivers.

The thermal $p\text{CO}_2$ component ($p\text{CO}_{2\ \text{T}}$) captures the changes in $p\text{CO}_2$ caused by seasonal temperature variations. Seasonal warming elevates surface $p\text{CO}_2$, whereas seasonal cooling reduces $p\text{CO}_2$ values due to changes in CO_2 gas solubility. The thermal $p\text{CO}_2$ component is computed in a similar fashion to $p\text{CO}_{2\ \text{AM}}$, but using the time-varying model fields of monthly SST and annual mean values of all other input parameters to isolate the effect of seasonal temperature changes on $p\text{CO}_2$ variability.

$$p\text{CO}_{2\ \text{T}} = f\left(\text{SST}, \overline{\text{SSS}}, \overline{\text{DIC}}, \overline{\text{TA}}, \overline{\text{PO}_4}, \overline{\text{Si}}\right) \tag{6}$$

This yields the simulated time series of the thermal $p\text{CO}_2$ component at monthly resolution. The efficacy with which seasonal SST variability alters the $p\text{CO}_{2\ \text{T}}$ seasonal cycle depends on the mean-state $p\text{CO}_{2\ \text{AM}}$ value, as each 1°C change in temperature exerts a ~4.23% change in $p\text{CO}_2$ (Takahashi et al., 1993). In other words, the $p\text{CO}_{2\ \text{AM}}$ governs the sensitivity of $p\text{CO}_2$ to seasonal temperature variations: higher $p\text{CO}_{2\ \text{AM}}$ values allow for the same seasonal SST variation to exert a larger influence on seasonal $p\text{CO}_2$ variability.

The residual, biophysical $p\text{CO}_2$ component ($p\text{CO}_{2\ \text{BP}}$) accounts for all other nonthermal carbon cycle processes, including air-sea CO_2 exchange, organic matter production and remineralization, calcium carbonate cycling, water mass mixing, and freshwater exchange. In the analysis by Rodgers et al. (2023), open-ocean biophysical $p\text{CO}_2$ seasonality in GOBMs was found to be primarily driven by seasonal DIC variations, with seasonal salinity and total alkalinity variations exerting minor controls (their Figure 7). For this reason, we conceptualize the structure and phasing of the biophysical $p\text{CO}_2$ seasonal cycle as primarily driven by that of the DIC seasonal cycle. Increased levels of primary production coincident with shoaling mixed layers in spring and summer reduce surface $p\text{CO}_2$ and DIC, while deep winter mixing introduces subsurface waters with high $p\text{CO}_2$ and respired DIC into the upper ocean. To ensure internal consistency with the simulated $p\text{CO}_2$ seasonal cycle within each model, we follow the procedure used by Rodgers et al. (2023) to compute the time series of $p\text{CO}_{2\ \text{BP}}$ as the difference between the $p\text{CO}_2$ time series and the seasonal $p\text{CO}_{2\ \text{T}}$ anomaly, computed using the time series of $p\text{CO}_{2\ \text{T}}$ and $p\text{CO}_{2\ \text{AM}}$.

$$p\text{CO}_{2\ \text{BP}} = p\text{CO}_2 - (p\text{CO}_{2\ \text{T}} - p\text{CO}_{2\ \text{AM}}) \tag{7}$$

As seasonal DIC variations predominantly control $p\text{CO}_{2\ \text{BP}}$ seasonal cycles, we describe the efficiency of the $p\text{CO}_2$ response to seasonal biophysical processes using the annual mean Revelle Factor (RF_{AM}), which represents the sensitivity of $p\text{CO}_2$ to seasonal changes in DIC (Broecker et al., 1979; Egleston et al., 2010; Fassbender et al., 2017; Revelle & Suess, 1957). The Revelle Factor is often discussed in the context of the surface ocean buffer capacity for C_{ant} accumulation, where waters with low RF values can more efficiently absorb anthropogenic CO_2 from the atmosphere, resulting in relatively smaller $p\text{CO}_2$ changes. This same concept of $p\text{CO}_2$ sensitivity also applies to seasonal carbon cycling, where waters with lower RF_{AM} values experience smaller relative changes in seasonal $p\text{CO}_2$ variability for the same seasonal DIC variation (Fassbender et al., 2018). The reverse is true for waters characterized by higher RF_{AM}.

While the timing of seasonal thermal $p\text{CO}_2$ and biophysical $p\text{CO}_2$ variations typically oppose each other, they are not often of the same magnitude or entirely out of phase (Figure 1). There is a well-known geographic distribution of the relative influence of thermal and biophysical processes on $p\text{CO}_2$ such that seasonal temperature changes dominate $p\text{CO}_2$ seasonality in mid-latitude regions (seasonal $p\text{CO}_2$ low in winter), in contrast to high-latitude subpolar regions and low-latitude equatorial regions that are more influenced by seasonal DIC changes (seasonal $p\text{CO}_2$ low in summer; Fassbender et al., 2018; Takahashi et al., 2002). The seasonal phasing of the overall $p\text{CO}_2$ cycle will align with that of its dominating driver.

We compute the seasonal cycle amplitudes of the thermal and biophysical $p\text{CO}_2$ components SST and DIC as well as their changes associated with C_{ant} accumulation and physical climate forcing following Equations 1–4 to evaluate the mechanisms of total A-$p\text{CO}_2$ change (Table 2). The seasonal $p\text{CO}_2$ decomposition and Revelle Factor computations were performed using CO2SYS Version 3.1.2 for MATLAB (Lewis & Wallace, 1998; Sharp et al., 2020; van Heuven et al., 2011). We use the dissociation constants for the carbonate system by Lueker et al. (2000), hydrogen sulfate by Dickson et al. (1990), and hydrogen fluoride by Perez and Fraga (1987) and the total boron-to-chlorinity ratio of Lee et al. (2010). Colormaps for figures are sourced from the cmocean MATLAB package (Thyng et al., 2016).

2.4. Interpreting Mechanisms of $p\mathrm{CO_2}$ Seasonal Amplitude Change

Changes in seasonal $p\mathrm{CO_2}$ amplitudes reflect alterations of seasonal variability drivers as well as changes in the annual mean-state surface conditions, which are captured by the thermal and biophysical component seasonal cycles (Figure 1). Expansions or contractions in the seasonal amplitudes of the thermal (A-$p\mathrm{CO_{2\ T}}$) and biophysical (A-$p\mathrm{CO_{2\ BP}}$) components can occur either from changes in the magnitude of seasonal SST or DIC variability (x axes of Figures 1b and 1c), or from changes in the sensitivity of $p\mathrm{CO_2}$ to those drivers, as regulated by $p\mathrm{CO_{2\ AM}}$ and $\mathrm{RF_{AM}}$, respectively (y axes of Figures 1b and 1c). The direction of sloping contours emphasizes that altering either the seasonal variability drivers or the sensitivity factors produces nonlinear changes in the seasonal amplitude of each $p\mathrm{CO_2}$ component. In this sense, for a given driver change, the initial conditions influence the magnitude of the seasonal $p\mathrm{CO_2}$ component response. For example, rising ocean carbon content due to $\mathrm{C_{ant}}$ accumulation directly elevates the sensitivity of $p\mathrm{CO_2}$ to thermal and biophysical processes by increasing the $p\mathrm{CO_{2\ AM}}$ and $\mathrm{RF_{AM}}$ (i.e., reduction in ocean buffering). This process is represented by the vertical arrows in Figures 1b and 1c. However, the resulting magnitude of thermal or biophysical $p\mathrm{CO_2}$ amplitude change depends on the initial baseline conditions. Surface waters characterized by a larger initial seasonal cycle amplitude of SST or DIC (black arrows) have a larger initial thermal or biophysical $p\mathrm{CO_2}$ component amplitude and will experience proportionally larger $\mathrm{C_{ant}}$-driven increases in the $p\mathrm{CO_2}$ component amplitude, compared to surface waters with smaller seasonality driver amplitudes (yellow arrows). This is visualized as the black vertical arrows crossing more A-$p\mathrm{CO_2}$ component contours. In a similar way, the initial sensitivity terms (y axes) influence how strongly $p\mathrm{CO_2}$ components respond to the same seasonal driver variability. In our analysis, we independently quantify how $\mathrm{C_{ant}}$ accumulation and changes in climate affect the seasonal amplitudes of SST and DIC as well as the $p\mathrm{CO_{2\ AM}}$ and $\mathrm{RF_{AM}}$ sensitivity factors to elucidate their combined role in causing differing seasonal $p\mathrm{CO_2}$ amplitude changes between GOBMs.

3. Results and Discussion

3.1. Decadal Changes in $p\mathrm{CO_2}$ Seasonal Cycle Amplitude Change

We present the changes in A-$p\mathrm{CO_2}$ and its thermal and biophysical components between 1980–1984 and 2014–2018 for one model (CESM-ETHZ) to illustrate the spatial patterns of change. In this model (Figure 2), the total change in seasonal $p\mathrm{CO_2}$ amplitude (Δ_{total} A-$p\mathrm{CO_2}$) ranged from −26 to 55 µatm (global mean = 6.8 µatm), with the largest increases over much of the subtropical and northern subpolar regions (Figure 2b). The total A-$p\mathrm{CO_2}$ change is near zero or negative in low latitudes and some areas of the Southern Ocean. Much of the total A-$p\mathrm{CO_2}$ increase can be attributed to $\mathrm{C_{ant}}$ accumulation in the water column (Δ_{Cant} A-$p\mathrm{CO_2}$; Figure 2c). The spatial pattern of $\mathrm{C_{ant}}$-driven change in A-$p\mathrm{CO_2}$ aligns with the 1980–1984 pattern of A-$p\mathrm{CO_2}$ (Figures 2a and 2c), with larger increases in northern subtropical and subpolar regions that experience naturally high seasonal $p\mathrm{CO_2}$ amplitudes. In contrast to the effect of $\mathrm{C_{ant}}$, the impact of changes in physical climate on A-$p\mathrm{CO_2}$ is spatially heterogeneous (Δ_{clim} A-$p\mathrm{CO_2}$, Figure 2d) and can locally enhance (when positive) or dampen (when negative) the $\mathrm{C_{ant}}$-driven A-$p\mathrm{CO_2}$ increase. Reductions in total A-$p\mathrm{CO_2}$ (Figure 2b) occur where the negative effect of changing climate (Figure 2d) outweighs the $\mathrm{C_{ant}}$-driven amplification (Figure 2c).

To further disentangle the mechanisms responsible for the overall A-$p\mathrm{CO_2}$ changes (Figure 2), the signals are decomposed into changes in the seasonal cycle amplitudes of the thermal (A-$p\mathrm{CO_{2\ T}}$) and biophysical (A-$p\mathrm{CO_{2\ BP}}$) components in this same model (Figure 3). The total changes in A-$p\mathrm{CO_{2\ T}}$ (global mean = 9.9 µatm; Figure 3a) often exceed the total A-$p\mathrm{CO_{2\ BP}}$ changes (global mean = 6.9 µatm; Figure 3d), particularly across mid-latitude regions. Consistent with the overall A-$p\mathrm{CO_2}$ (Figure 2), $\mathrm{C_{ant}}$-driven changes in A-$p\mathrm{CO_{2\ T}}$ and A-$p\mathrm{CO_{2\ BP}}$ (Figures 3b and 3e) are generally larger than those driven by climate (Figures 3c and 3f). Local climate effects modulate $\mathrm{C_{ant}}$-driven amplifications, especially for the biophysical $p\mathrm{CO_2}$ component in mid- and low-latitudes (Figure 3f), where the $\mathrm{C_{ant}}$-driven A-$p\mathrm{CO_{2\ BP}}$ signal is relatively weak. The opposing phasing of the thermal and biophysical $p\mathrm{CO_2}$ components (e.g., Figure 1a) means that their competing changes determine both the spatial structure and net magnitude of the overall A-$p\mathrm{CO_2}$ changes shown in Figure 2.

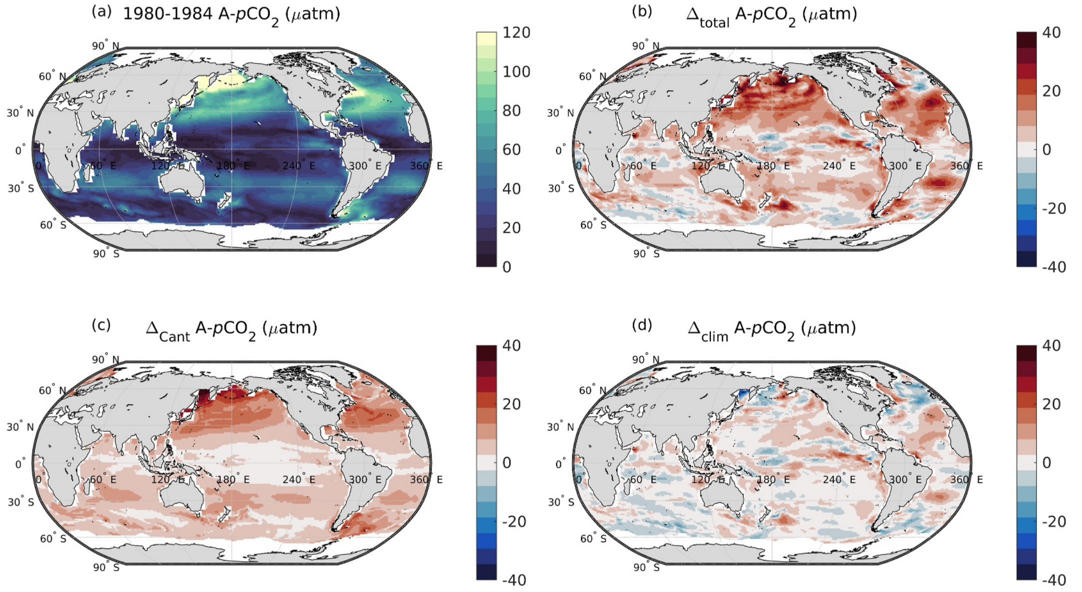

Figure 2. (a) The 1980–1984 mean $p\mathrm{CO}_2$ seasonal cycle amplitude (A-$p\mathrm{CO}_2$) in a representative global ocean biogeochemical model (CESM-ETHZ; Lindsay et al., 2014; Yang & Gruber, 2016) and (b) the total change in A-$p\mathrm{CO}_2$ between 1980-1984 and 2014–2018. The total change is attributed to the changes caused by (c) anthropogenic carbon accumulation (Δ_{Cant} A-$p\mathrm{CO}_2$) and (d) changes in physical climate (Δ_{clim} A-$p\mathrm{CO}_2$).

3.1.1. Mechanisms of $p\mathrm{CO}_2$ Seasonal Cycle Amplitude Change

The separation of seasonal $p\mathrm{CO}_2$ variability into thermal and biophysical components helps clarify the relative roles of changes in mean-state sensitivity factors ($p\mathrm{CO}_{2\ \mathrm{AM}}$ and $\mathrm{RF}_{\mathrm{AM}}$) and seasonal variability drivers (SST and DIC) in seasonal $p\mathrm{CO}_2$ component responses to $\mathrm{C}_{\mathrm{ant}}$ and climate perturbations (Figure 4; see Section 2.4).

$\mathrm{C}_{\mathrm{ant}}$-driven increases in A-$p\mathrm{CO}_{2\ \mathrm{T}}$ and A-$p\mathrm{CO}_{2\ \mathrm{BP}}$ (Figures 3b and 3e) are primarily due to the enhanced $p\mathrm{CO}_2$ sensitivity to seasonal SST and DIC variations (Figures 4a and 4b), with small or negligible $\mathrm{C}_{\mathrm{ant}}$-driven changes to the seasonal SST and DIC cycles themselves (Figure S2 in Supporting Information S1). For the thermal $p\mathrm{CO}_2$ component, $\mathrm{C}_{\mathrm{ant}}$ accumulation increases surface $p\mathrm{CO}_{2\ \mathrm{AM}}$ values relatively uniformly (Figure 4a) and does not directly alter the seasonal SST cycle (Figure S2 in Supporting Information S1). Thus, $\mathrm{C}_{\mathrm{ant}}$-induced thermal component amplifications (Figure 3b) can be fully explained by an increased sensitivity to the underlying SST seasonality via increasing $p\mathrm{CO}_{2\ \mathrm{AM}}$ (Figure 4a), with spatial distributions of $\mathrm{C}_{\mathrm{ant}}$-driven A-$p\mathrm{CO}_{2\ \mathrm{T}}$ changes scaling the 1980-1984 A-SST distributions. Northern subtropical regions experience larger $\mathrm{C}_{\mathrm{ant}}$-driven A-$p\mathrm{CO}_{2\ \mathrm{T}}$ responses, where seasonal SST variations are naturally larger. For the biophysical $p\mathrm{CO}_2$ component, $\mathrm{C}_{\mathrm{ant}}$ accumulation reduces the ocean buffer capacity (increases $\mathrm{RF}_{\mathrm{AM}}$; Figure 4b) and additionally weakens the seasonal DIC amplitude in parts of the Southern Ocean and subpolar Northern Hemisphere (Figure S2 in Supporting Information S1). $\mathrm{RF}_{\mathrm{AM}}$ values increase globally, translating to a heightened $p\mathrm{CO}_2$ sensitivity to seasonal DIC variations. The largest $\mathrm{RF}_{\mathrm{AM}}$ increases occur in high-latitude subpolar waters compared to lower latitude regions (Egleston et al., 2010; Fassbender et al., 2017; Takahashi et al., 1980). Further, although reductions in seasonal DIC amplitudes in high latitudes can slightly dampen A-$p\mathrm{CO}_{2\ \mathrm{BP}}$, the $\mathrm{C}_{\mathrm{ant}}$-induced decrease in A-DIC over this time period is relatively small (<10% since 1980–1984; Figure S4 in Supporting Information S1). Thus, the spatial patterns of $\mathrm{C}_{\mathrm{ant}}$-driven A-$p\mathrm{CO}_{2\ \mathrm{BP}}$ increases (Figure 3e) primarily reflect the enhanced sensitivity of $p\mathrm{CO}_2$ to underlying seasonal DIC variations via increasing $\mathrm{RF}_{\mathrm{AM}}$ (Figure 4b). The largest $\mathrm{C}_{\mathrm{ant}}$-driven A-$p\mathrm{CO}_{2\ \mathrm{BP}}$ responses occur where the 1980-1984 A-DIC and the $\mathrm{C}_{\mathrm{ant}}$-driven increases in $\mathrm{RF}_{\mathrm{AM}}$ are large. This is seen in high-latitude subpolar regions, particularly in the Northern Hemisphere.

Climate-state-driven changes to A-$p\mathrm{CO}_{2\ \mathrm{T}}$ and A-$p\mathrm{CO}_{2\ \mathrm{BP}}$ (Figures 3c and 3f) are primarily due to changes in seasonal SST and DIC amplitudes (Figures 4c and 4d), with smaller contributions from changes in sensitivity factors (Figure S2 in Supporting Information S1). As $\mathrm{C}_{\mathrm{ant}}$ accumulation alone does not alter SST seasonality, changes in A-SST between 1980 and 2018 are associated with changes in climate state (Figure 4c). Similarly,

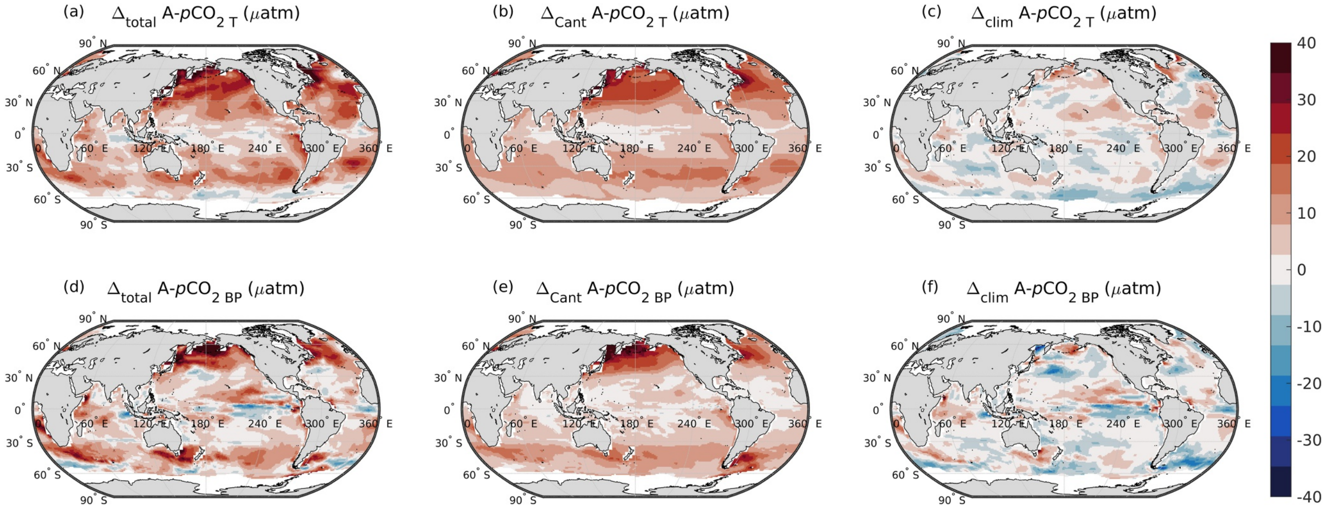

Figure 3. Change in the seasonal cycle amplitude (A) of the (a–c) thermal (A-$p\text{CO}_{2\ \text{T}}$) and (d–f) biophysical (A-$p\text{CO}_{2\ \text{BP}}$) components of $p\text{CO}_2$ between 1980–1984 and 2014–2018 as simulated by CESM-ETHZ. Panels show the (a, d) total change (Δ_{total}) and the contributions from (b, e) anthropogenic carbon accumulation (Δ_{Cant}), and (c, f) changes in physical climate (Δ_{clim}).

climate-induced changes in A-DIC are relatively large near the equator and in low latitudes (Figure 4d) and are responsible for the majority of the total A-DIC change in those regions. Because the climate-driven changes in sensitivity factors are relatively minor (Figure S2 in Supporting Information S1), the spatial variability in climate-induced changes in A-$p\text{CO}_{2\ \text{T}}$ and A-$p\text{CO}_{2\ \text{BP}}$ (Figures 3c and 3f) is similar to that in A-SST and A-DIC, respectively (Figures 4c and 4d).

In summary, the decadal changes in A-$p\text{CO}_2$ and its thermal and biophysical components are primarily caused by C_{ant} accumulation and the resulting enhancement in $p\text{CO}_2$ sensitivity to underlying seasonal thermal and biophysical processes via increases in $p\text{CO}_{2\ \text{AM}}$ and RF_{AM} (Figures 2–4). Near the equator and in some regions of the Southern Ocean, the effect of changes in climate on A-$p\text{CO}_2$ via A-SST and A-DIC alterations may outweigh the seasonal $p\text{CO}_2$ amplification caused by C_{ant}. The total A-$p\text{CO}_{2\ \text{T}}$ increase is greater than that of A-$p\text{CO}_{2\ \text{BP}}$ in

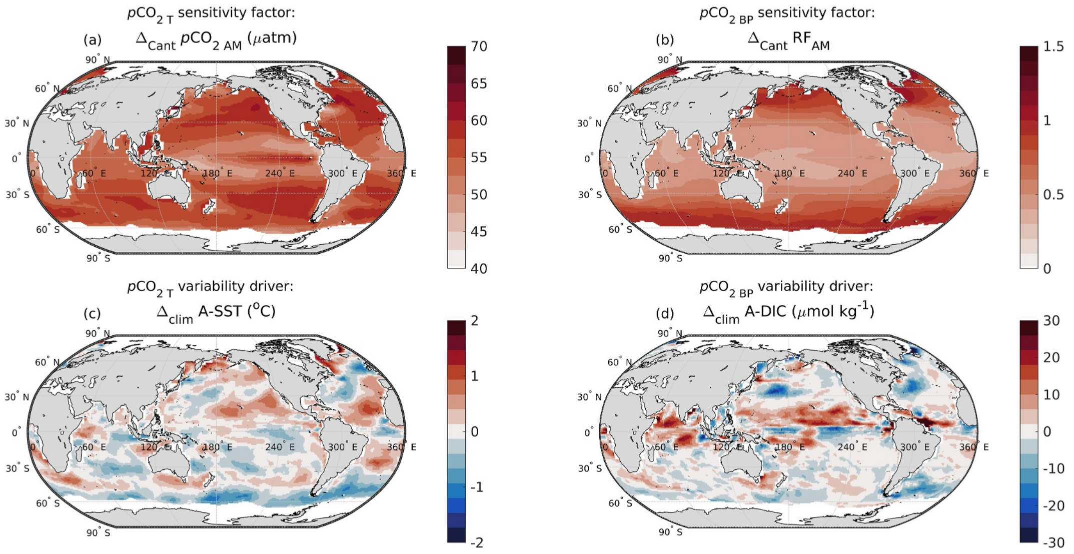

Figure 4. Changes in the mean-state sensitivity factors and seasonal variability drivers that dictate $p\text{CO}_2$ component seasonality changes. Panels show the changes due to anthropogenic carbon accumulation (Δ_{Cant}) for the (a) annual mean $p\text{CO}_2$ ($p\text{CO}_{2\ \text{AM}}$) value and (b) annual mean Revelle Factor (RF_{AM}), and the changes associated with changing physical climate states (Δ_{clim}) for the seasonal cycle amplitude (A) of (c) SST and (d) DIC.

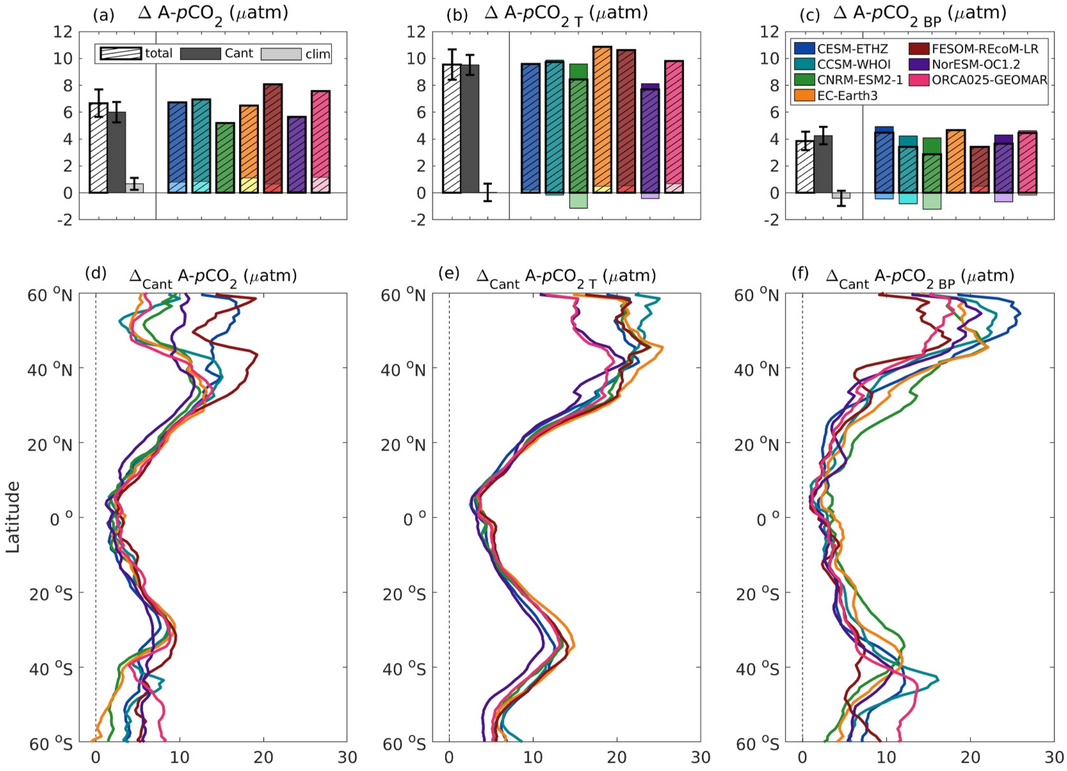

Figure 5. Area-normalized global mean changes in the (a) surface ocean $p\text{CO}_2$ seasonal cycle amplitude (ΔA-$p\text{CO}_2$) from 1980–1984 to 2014–2018 and its decomposition into changes in the (b) thermal (ΔA-$p\text{CO}_{2\ \text{T}}$) and (c) biophysical (ΔA-$p\text{CO}_{2\ \text{BP}}$) $p\text{CO}_2$ seasonal cycle components. In panels (a–c), GOBM ensemble-mean ($n = 7$) changes are shown in grayscale, with error bars representing ±1 standard deviation, and individual GOBMs are shown in color. The total amplitude change (hashed) is separated into its contributions from anthropogenic carbon accumulation (C_{ant}, dark shading) and changes in climate state (clim, light shading). Area-normalized zonally averaged changes associated with total C_{ant} accumulation (Δ_{Cant}) to (d) A-$p\text{CO}_2$, (e) A-$p\text{CO}_{2\ \text{T}}$, and (f) A-$p\text{CO}_{2\ \text{BP}}$ for individual GOBMs. Sea ice regions (Arctic and subpolar Southern Ocean) are excluded from the global and zonal averaging.

much of the surface ocean, owing to a larger increase caused by C_{ant} and a smaller opposing effect of climate-state change when globally integrated (Figure 3). These findings agree with those from Rodgers et al. (2023), which employs a complementary approach to attribute anthropogenic changes in $p\text{CO}_2$ seasonality using the same GOBMs, and with 21st-century projections of $p\text{CO}_2$ seasonality change made using ESMs (Fassbender et al., 2022; Gallego et al., 2018). While we have described the mechanisms behind A-$p\text{CO}_2$ change in one model (CESM-ETHZ; Figures 2–4), the same processes hold for all models (Figure 5). In the ensemble mean, GOBMs simulate a globally averaged total increase in A-$p\text{CO}_2$ of 6.6 ± 1.1 μatm, with 5.9 ± 0.6 μatm increase caused by C_{ant} accumulation and 0.7 ± 0.5 μatm increase due to changes in physical climate, over the nearly 40-year period (Figure 5a). On average, the C_{ant} response is strengthened by changes caused by climate over recent decades, though the fractional contribution of climate is inconsistent across models (Figures 5a–5c).

3.2. Across-Model Differences in C_{ant}-Driven $p\text{CO}_2$ Seasonal Cycle Amplitude Change

Given that decadal changes in A-$p\text{CO}_2$ and its thermal and biophysical components are primarily driven by C_{ant} accumulation in all models (Figure 5), we next examine what contributes to differences across models in the magnitude of C_{ant}-driven $p\text{CO}_2$ amplification. Although across-model differences in the climate response can help explain the contrasting spatial patterns of total A-$p\text{CO}_2$ change (Figure S5 in Supporting Information S1), the global-mean contribution of climate-forced alterations is comparatively small (Figures 5a–5c). Thus, we focus on the C_{ant}-driven changes, as this process will intensify with continued fossil fuel emissions and remain the dominant anthropogenic signal influencing $p\text{CO}_2$ seasonality over time (e.g., Fassbender et al., 2022; Gallego et al., 2018).

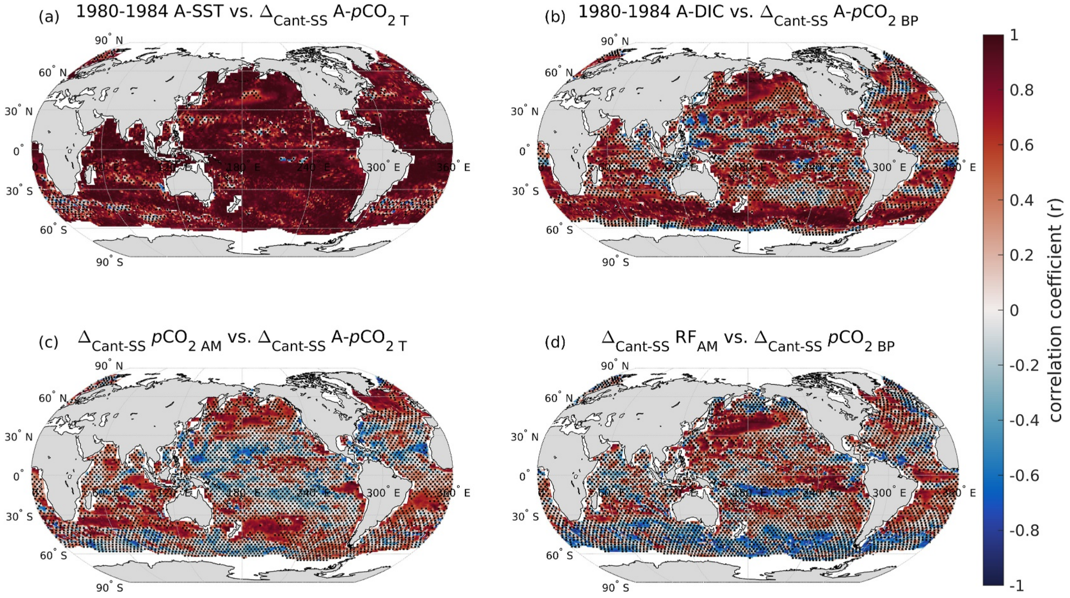

Figure 6. Local across-model correlation coefficients for regressions of (a) 1980–1984 A-SST versus $\Delta_{\text{Cant-SS}}$ A-$p\text{CO}_{2\ \text{T}}$, (b) 1980-1984 A-DIC versus $\Delta_{\text{Cant-SS}}$ A-$p\text{CO}_{2\ \text{BP}}$, (c) $\Delta_{\text{Cant-SS}}$ $p\text{CO}_{2\ \text{AM}}$ versus $\Delta_{\text{Cant-SS}}$ A-$p\text{CO}_{2\ \text{T}}$, and (d) $\Delta_{\text{Cant-SS}}$ RF_{AM} versus $\Delta_{\text{Cant-SS}}$ A-$p\text{CO}_{2\ \text{BP}}$. $\Delta_{\text{Cant-SS}}$ represents the steady-state response to anthropogenic carbon accumulation by rising atmospheric CO_2 in *Simulation C*. Models with higher (lower) initial A-SST or A-DIC render a correspondingly larger (smaller) $\text{C}_{\text{ant-SS}}$-induced change in A-$p\text{CO}_{2\ \text{T}}$ or A-$p\text{CO}_{2\ \text{BP}}$. Black stippling indicates where relationships are insignificant ($p > 0.15$).

Models broadly agree on the latitudinal structure of C_{ant}-driven expansions in $p\text{CO}_2$ seasonal amplitudes; however, there are notable regional disagreements between models, as reflected in the zonal mean C_{ant}-driven changes in A-$p\text{CO}_2$ and its components (Figures 5d–5f). Models simulate similar magnitudes of C_{ant}-driven change in tropical and subtropical latitudes (30°S to 30°N) where background $p\text{CO}_2$ seasonality is small, but this agreement breaks down moving toward temperate and subpolar latitudes, particularly for the biophysical component (Figure 5f). Prior studies evaluating across-model differences in annual anthropogenic air-sea CO_2 fluxes have emphasized the role of model biases in mean-state sensitivity factors, namely $p\text{CO}_{2\ \text{AM}}$ and RF_{AM} (e.g., Terhaar et al., 2022). Here, we highlight the additional role of biases in seasonal variability drivers in causing across-model disagreements in C_{ant}-induced A-$p\text{CO}_2$ change and ultimately seasonal sea-air CO_2 fluxes. To isolate this effect, we hereafter consider the steady-state impact of rising atmospheric CO_2 alone (denoted as $\text{C}_{\text{ant-SS}}$) in altering $p\text{CO}_2$ seasonal cycles and its drivers using *Simulation C* (Equation 3; Table 2). This excludes the small, heterogeneous influence of non-steady-state interactions between C_{ant} and changing climate states (Figure S6 in Supporting Information S1).

Across-model disagreements in C_{ant}-driven changes in $p\text{CO}_2$ component amplitudes can be explained by (a) different magnitudes of increase in mean-state sensitivity factors ($p\text{CO}_{2\ \text{AM}}$ and RF_{AM}) and (b) different initial seasonal SST and DIC variations themselves (Figure 6). Under rising atmospheric CO_2 alone, seasonal SST variations remain unaltered from initialized conditions, and DIC seasonal cycles experience regionally small C_{ant}-driven changes over the study period (Figures S2 and S4 in Supporting Information S1). Thus, each model's 1980–1984 spatial structure and magnitude of A-SST and A-DIC respectively govern A-$p\text{CO}_{2\ \text{T}}$ and A-$p\text{CO}_{2\ \text{BP}}$ patterns over time, incorporating systematic biases from post spin-up conditions. Models that are biased high (low) in their initialized A-SST or A-DIC simulate persistently larger (smaller) A-$p\text{CO}_{2\ \text{T}}$ or A-$p\text{CO}_{2\ \text{BP}}$ growth caused by C_{ant}, indicated by high positive correlation coefficients for the across-model values (Figures 6a and 6b). For each grid cell, we derive the local relationship by computing the correlation coefficient (r) across models between the 1980–1984 A-SST and A-DIC values and the corresponding $\text{C}_{\text{ant-SS}}$-driven $p\text{CO}_2$ component change. These relationships are nearly global for both the thermal (global mean $r \pm 1\sigma = 0.82 \pm 0.25$) and biophysical (global mean $r \pm 1\sigma = 0.44 \pm 0.40$) $p\text{CO}_2$ components (Figures 6a and 6b). Patchy relationships between 1980–1984 A-DIC and $\text{C}_{\text{ant-SS}}$-driven changes in A-$p\text{CO}_{2\ \text{BP}}$ near the equator and in mid-latitudes (Figure 6b) indicate where A-$p\text{CO}_{2\ \text{BP}}$ changes are small (Figure 5f) and/or where surface seasonal salinity or total alkalinity cycles may be locally important.

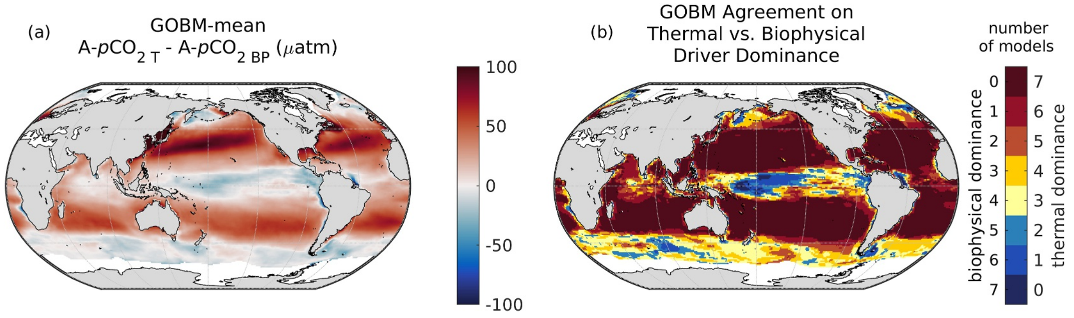

Figure 7. (a) GOBM ensemble-mean ($n = 7$) difference between A-$pCO_{2\ T}$ and A-$pCO_{2\ BP}$ averaged over 1980–2018 in *Simulation C*. Positive values indicate where thermal processes dominate over biophysical processes (vice versa). (b) Categorical map reflecting the number of models in agreement that thermal processes (reds, lower winter surface pCO_2) or biophysical processes (blues, higher winter surface pCO_2) dominate the local pCO_2 seasonal cycle. Yellow areas delineate regions with the largest inter-model disagreement in the dominating driver.

Across-model differences in $C_{ant\text{-}SS}$-driven changes in $pCO_{2\ AM}$ and RF_{AM} appear to correlate positively with thermal and biophysical changes over much of the open ocean (Figures 6c and 6d), but these relationships are weaker compared to those with the 1980-1984 A-SST and A-DIC. Models show rather consistent meridional patterns in $C_{ant\text{-}SS}$-driven changes in $pCO_{2\ AM}$ and RF_{AM} and display much larger differences in their initial A-SST and A-DIC conditions (Figure S7 in Supporting Information S1). Therefore, while enhanced pCO_2 sensitivity is the dominant mechanism behind $C_{ant\text{-}}$-driven pCO_2 amplification, our results suggest that the initial magnitudes and spatial patterns of A-SST and A-DIC predominantly cause the across-model differences in thermal and biophysical pCO_2 amplifications, respectively. Accordingly, models with larger 1980-1984 A-pCO_2 exhibit proportionally larger C_{ant}-driven A-pCO_2 increases (Figure S8 in Supporting Information S1). This finding indicates that the spread in A-pCO_2 between models increases over time, primarily due to across-model differences in initial A-SST and A-DIC conditions (Figure S9 in Supporting Information S1).

The local magnitude of C_{ant}-driven A-pCO_2 change in each model reflects the superposition of competing A-$pCO_{2\ T}$ and A-$pCO_{2\ BP}$ changes. Thus, the across-model differences in seasonal pCO_2 amplifications are additionally linked to the spatial pattern of thermal versus biophysical seasonal variability driver dominance. We quantify the dominant driver by taking the difference between the A-$pCO_{2\ T}$ and A-$pCO_{2\ BP}$ (Takahashi et al., 2002), averaged over the analysis period in *Simulation C* (1980–2018; Figure 7a). Although the dominant driver could change over time if pCO_2 component amplitudes increase at different rates, all models maintain the same internal dominant driver throughout the simulation (Figure S10 in Supporting Information S1). All considered models agree on thermal dominance in the subtropical gyres (Figure 7b), where A-$pCO_{2\ T}$ is larger than A-$pCO_{2\ BP}$ (Figure 7a), reflecting that models agree on the seasonal pCO_2 phasing (winter pCO_2 lows and summer pCO_2 highs). In contrast, inconsistencies in the dominant driver emerge over northern subpolar gyres and in parts of the equatorial regions and Southern Ocean (yellow regions in Figure 7b). In these regions, biophysical processes are expected to dominate, and surface pCO_2 is expected to have seasonal phasing opposite to the subtropics. Disagreement on the spatial extent of biophysical dominance indicates that the models represent seasonal carbon cycle processes differently, particularly in high-latitude subpolar regions. Rodgers et al. (2023) showed that, on average, GOBMs underestimate the magnitude of mean-state A-DIC relative to observation-based estimates over much of the surface ocean. This leads to a widespread bias toward thermal dominance in most models (their Figure 6; Figure S10 in Supporting Information S1), resulting in a systematically larger C_{ant}-driven thermal pCO_2 amplification (Figure 5). Thus, biases in seasonal DIC variability contribute to persistent across-model discrepancies in the magnitude and spatial pattern of C_{ant}-driven pCO_2 amplification.

3.3. Relevance to Seasonal Sea-Air CO_2 Fluxes and Cumulative Ocean Carbon Sink Strength

Alterations to surface pCO_2 seasonal cycles can influence the strength of the annual ocean carbon sink by altering the seasonality of the sea-air pCO_2 gradient. Since atmospheric pCO_2 is relatively well mixed and exhibits comparatively weak seasonality, surface pCO_2 variations predominantly determine the timing and magnitude of sea-air CO_2 fluxes and ocean C_{ant} uptake. Accordingly, $C_{ant\text{-}SS}$-driven amplification of surface pCO_2 results in the amplification of seasonal sea-air pCO_2 disequilibrium ($\Delta pCO_2^{\text{sea-air}}$) over much of the middle and high latitudes

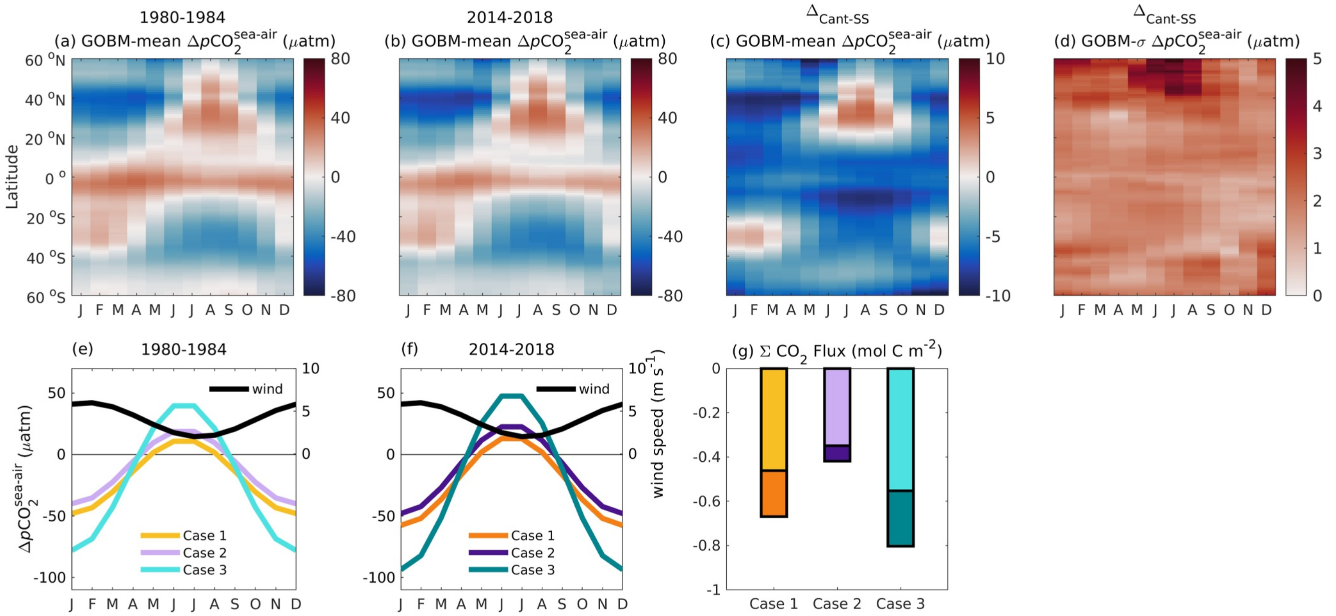

Figure 8. Hovmöller plots showing the GOBM ensemble-mean zonal averages of the sea-air $p\text{CO}_2$ disequilibrium ($\Delta p\text{CO}_2^{\text{sea-air}}$) in (a) 1980–1984 and (b) 2014–2018 and (c) the steady-state anthropogenic-carbon-induced change ($\Delta_{\text{Cant-SS}}$; *Simulation C*) between the two periods. In (a) and (b), negative values represent ocean carbon uptake. (d) The $\text{C}_{\text{ant-SS}}$-driven change in the across-model standard deviation of $\Delta p\text{CO}_2^{\text{sea-air}}$. Theoretical $\Delta p\text{CO}_2^{\text{sea-air}}$ seasonal cycles representative of a thermally dominated region of the Northern Hemisphere for the (e) 1980–1984 and (f) 2014–2018 periods, with seasonal wind speeds (black line). Case 1 (oranges) and Case 2 (purples) simulate identical seasonal amplitudes of $\Delta p\text{CO}_2^{\text{sea-air}}$, but Case 2 has a higher annual mean value (+8 µatm). Case 1 and Case 3 (teals) simulate identical annual mean $\Delta p\text{CO}_2^{\text{sea-air}}$, but Case 3 has a larger seasonal cycle amplitude (2x larger). The 20% increase in amplitudes between (e) and (f) represents the impact of $\text{C}_{\text{ant-SS}}$ accumulation. (g) Theoretical cumulative annual ocean CO_2 flux ($\sum\text{CO}_2$ flux) for each period computed using seasonal $\Delta p\text{CO}_2^{\text{sea-air}}$ and winds from (e, f), with the gas transfer parameterization by Wanninkhof (2014). Negative values represent ocean carbon uptake.

(>20°N and <20°S; Figures 8a–8c), resulting in higher highs and lower lows annually. Near the equator and in high latitudes, $\Delta p\text{CO}_2^{\text{sea-air}}$ decreases in all seasons due to $\text{C}_{\text{ant-SS}}$, suggesting that the rise in atmospheric CO_2 outpaces the rise in surface $p\text{CO}_2$ throughout the year. Furthermore, persistent seasonal driver biases lead to an increasing across-model spread in the $\text{C}_{\text{ant-SS}}$-driven change to seasonal $\Delta p\text{CO}_2^{\text{sea-air}}$ values globally, as reflected by the increases in inter-model standard deviations (Figure 8d). This pattern indicates that models biased toward larger seasonal $\Delta p\text{CO}_2^{\text{sea-air}}$ amplitudes in 1980–1984 exhibit larger $\text{C}_{\text{ant-SS}}$-driven growth over time (Figure S11 in Supporting Information S1). The largest increases in the across-model spread of seasonal $\Delta p\text{CO}_2^{\text{sea-air}}$ are found at high northern hemisphere latitudes (>40°N), particularly in summer, where models considerably disagree on the dominant $p\text{CO}_2$ driver and surface $p\text{CO}_2$ phasing (Figure 7b).

It is important to note that an increase in the seasonal amplitude of surface $p\text{CO}_2$ or $\Delta p\text{CO}_2^{\text{sea-air}}$ may not always lead to a change in the net annual ocean carbon sink, particularly if changes in seasonal sea-air CO_2 flux compensate for one another. To evaluate the impact of C_{ant}-driven surface $p\text{CO}_2$ and $\Delta p\text{CO}_2^{\text{sea-air}}$ seasonal cycle changes on net CO_2 fluxes, variations in wind speeds must also be considered. C_{ant}-induced amplifications of $\Delta p\text{CO}_2^{\text{sea-air}}$ seasonality disproportionately enhance CO_2 fluxes during the season with maximum wind speeds, which generally occurs in winter when stronger winds enhance gas exchange efficiency (Fassbender et al., 2022). Because RECCAP2 did not include surface wind fields used by individual models, the role of seasonal wind variability in modulating CO_2 flux changes could not be directly evaluated in this study and remains a focus for future work. However, as the GOBMs are forced with reanalysis wind speeds constrained by real-world data, the spatial and temporal patterns of wind speeds are generally fixed across models. Thus, across-model differences in the phasing and magnitude of $\Delta p\text{CO}_2^{\text{sea-air}}$ should contribute significantly to across-model differences in seasonal CO_2 fluxes. The question is then whether these seasonal CO_2 flux differences can help explain historical annual ocean carbon sink differences among GOBMs. Before addressing this, we illustrate conceptually how biases in $p\text{CO}_2$ seasonality can work alongside annual mean-state biases to alter the annual ocean carbon sink under seasonally varying wind speeds (Figures 8e–8g).

In regions where the thermal $p\mathrm{CO}_2$ component dominates (e.g., subtropics), surface ocean $p\mathrm{CO}_2$ reaches a seasonal low during the colder winter months. The timing of this wintertime $p\mathrm{CO}_2$ low coincides with seasonally high wind speeds, making winter the dominant ocean CO_2 sink season in subtropical regions (e.g., Rodgers et al., 2008). In our example, we consider three different theoretical scenarios of $\Delta p\mathrm{CO}_2^{\text{sea-air}}$ with identical seasonal phasing but differing degrees of bias in seasonal amplitude and annual mean value (Figure 8e). Case 1 (oranges) and Case 2 (purples) exhibit the same seasonal amplitude of $\Delta p\mathrm{CO}_2^{\text{sea-air}}$, but Case 2 has a higher annual mean value (+8 μatm from Case 1). Case 1 and Case 3 (teals) exhibit the same annual mean $\Delta p\mathrm{CO}_2^{\text{sea-air}}$ value, but Case 3 has a larger seasonal cycle amplitude (2x larger than Case 1). In all scenarios, $\Delta p\mathrm{CO}_2^{\text{sea-air}}$ reaches a minimum in winter and a maximum in summer, reflecting thermal driver dominance. The more pronounced cycle in Case 3 represents a scenario with larger A-SST and correspondingly larger seasonal amplitude of $\Delta p\mathrm{CO}_2^{\text{sea-air}}$, whereas Case 1 and Case 2 represent weaker A-SST conditions. To mimic the effect of C_{ant} accumulation, we impose a 20% increase in the $\Delta p\mathrm{CO}_2^{\text{sea-air}}$ seasonal cycle for each scenario (Figure 8f) and compute the change in cumulative annual CO_2 flux under identical seasonal wind speeds (Figure 8g). Case 2, with a higher annual mean $\Delta p\mathrm{CO}_2^{\text{sea-air}}$, shows the smallest increase in cumulative annual CO_2 uptake, whereas Case 3, with the lowest wintertime $\Delta p\mathrm{CO}_2^{\text{sea-air}}$, shows the largest increase (Figure 8g). This occurs because stronger winter wind speeds enhance the impact of wintertime $\Delta p\mathrm{CO}_2^{\text{sea-air}}$ changes, giving greater efficacy to the CO_2 sink season in the scenario with larger SST seasonality.

Although this example considers the impact of C_{ant}-induced seasonal $\Delta p\mathrm{CO}_2^{\text{sea-air}}$ changes in the annual carbon sink in thermally dominated regions, the ocean carbon sink is expected to be enhanced globally by seasonal $p\mathrm{CO}_2$ changes in the GOBMs. Because GOBMs are systematically biased toward thermal dominance (Rodgers et al., 2023; Figure 7; Figure S10 in Supporting Information S1), the thermal $p\mathrm{CO}_2$ component amplification largely outcompetes the biophysical $p\mathrm{CO}_2$ component amplification (Figure 5). Consequently, in biophysically dominated regions where the seasonal $p\mathrm{CO}_2$ (and $\Delta p\mathrm{CO}_2^{\text{sea-air}}$) phasing is opposite, the simulated C_{ant}-induced increase in the wintertime $p\mathrm{CO}_2$ high is weaker than it should be. This inherent GOBM tendency toward thermal dominance strengthens the annual ocean carbon sink by increasing (reducing) the wintertime CO_2 influx (efflux) in thermally (biophysically) dominated regions (e.g., Fassbender et al., 2022). As a result, the growing disagreement in seasonal $\Delta p\mathrm{CO}_2^{\text{sea-air}}$ between models likely contributes to the increasing across-model spread in seasonal CO_2 fluxes and ultimately the cumulative global ocean carbon sink strength.

With this theoretical framework, we now evaluate how the simulated differences in C_{ant}-induced A-$p\mathrm{CO}_2$ and seasonal $\Delta p\mathrm{CO}_2^{\text{sea-air}}$ changes between GOBMs relate to across-model differences in the cumulative annual sea-air CO_2 fluxes ($\sum\mathrm{CO}_2$ Flux) over time (Figure 9). For each model, we compute the mean change in A-$p\mathrm{CO}_2$, $\Delta p\mathrm{CO}_2^{\text{sea-air}}$, and cumulative annual sea-air CO_2 flux driven by $\mathrm{C}_{\text{ant-SS}}$ invasion over consecutive 5-year increments, relative to their respective 1980–1984 mean starting values. This approach provides an estimate of how each parameter evolves over time within each model, smoothing for interannual variability. The local across-model correlation coefficients between the C_{ant}-driven changes in A-$p\mathrm{CO}_2$ and cumulative annual CO_2 flux do not show a fully coherent relationship over the analysis period (1980–1984 to 2014–2018 global mean $r \pm 1\sigma = -0.10 \pm 0.45$; Figure 9a). However, within each model, the time series of C_{ant}-driven changes in A-$p\mathrm{CO}_2$ and cumulative annual CO_2 fluxes are significantly negatively correlated (Figure S12 in Supporting Information S1), directly linking increases in A-$p\mathrm{CO}_2$ to stronger annual ocean carbon uptake within each internally consistent model framework. Decadal rates of carbon sink change range from -0.48 to -0.28 mol C m^{-2} decade^{-1} $\mu\mathrm{atm}^{-1}$ across models (Figure 9b; Table S1 in Supporting Information S1). These differences reflect model-specific biases in annual and seasonal carbon cycle representations, which obscure coherent local across-model relationships between C_{ant}-driven changes in A-$p\mathrm{CO}_2$ and cumulative annual CO_2 fluxes (Figure 9a).

We next evaluate the relationship between C_{ant}-driven changes in winter $\Delta p\mathrm{CO}_2^{\text{sea-air}}$ and cumulative annual CO_2 fluxes to highlight the role of wind speed seasonality in modulating seasonal sea-air CO_2 fluxes. Local across-model C_{ant}-driven changes in winter $\Delta p\mathrm{CO}_2^{\text{sea-air}}$ are tightly and positively correlated with changes in cumulative annual CO_2 flux over much of the ocean (Figure 9c; global mean $r \pm 1\sigma = 0.44 \pm 0.37$), indicating that models simulating larger winter $\Delta p\mathrm{CO}_2^{\text{sea-air}}$ decreases exhibit larger annual ocean carbon sink increases between 1980–1984 and 2014–2018. The seasonal alignment of strong winter winds with C_{ant}-driven reductions in $\Delta p\mathrm{CO}_2^{\text{sea-air}}$ enhances the seasonal ocean CO_2 sink and the net annual ocean carbon sink strength. While $\Delta p\mathrm{CO}_2^{\text{sea-air}}$ tends to decrease across all seasons outside of the subtropics (Figure 8c), changes in globally mean seasonal CO_2 fluxes are largest in winter (Figure S13 in Supporting Information S1). This mechanistic relationship between C_{ant}-driven $\Delta p\mathrm{CO}_2^{\text{sea-air}}$ and cumulative annual CO_2 flux changes in winter holds globally

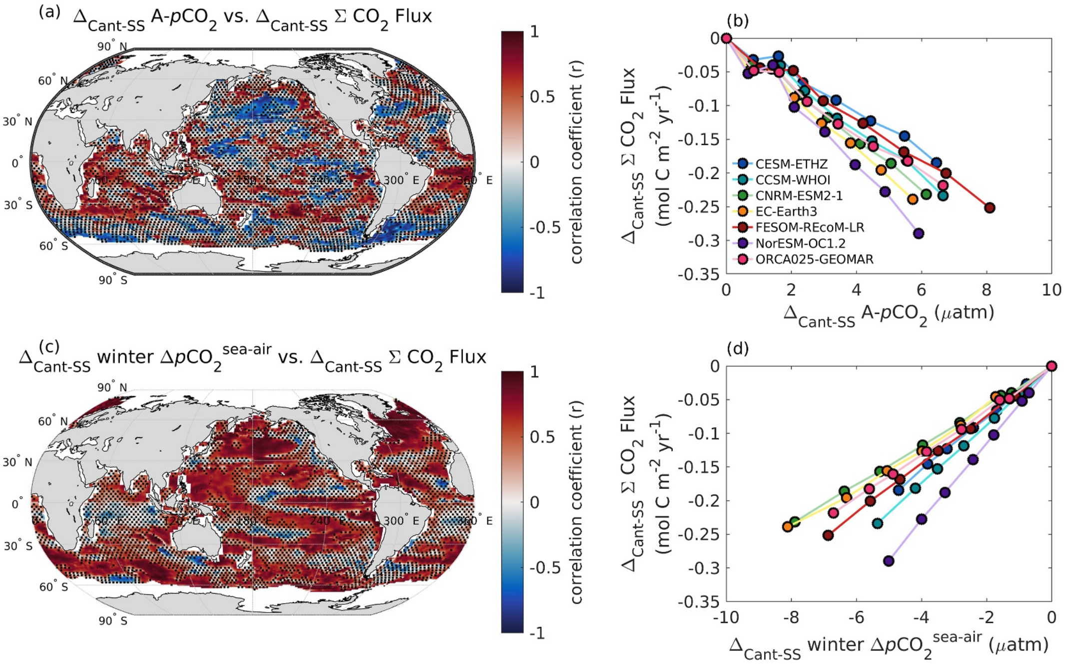

Figure 9. Across-model local correlation coefficients (r) for regressions of steady-state C_{ant}-induced changes ($\Delta_{Cant\text{-}SS}$) in cumulative annual CO_2 flux ($\sum CO_2$ flux) versus (a) A-pCO_2 or versus (c) the winter sea-air pCO_2 disequilibrium ($\Delta pCO_2^{sea\text{-}air}$) between 1980–1984 and 2014–2018. Winter is defined as January–March in the Northern Hemisphere and as June–August in the Southern Hemisphere. Black stippling indicates where relationships are insignificant ($p > 0.15$). Panels (b, d) show the area-weighted global mean relationships over time within each GOBM at five-year increments between 1980 and 2018 (colored circles). Negative values of $\Delta_{Cant\text{-}SS}$ $\sum CO_2$ flux (y-axes) indicate an increasing cumulative carbon sink over time. Sea ice regions (Arctic and subpolar Southern Ocean) are excluded from the global averaging.

within each model (Figure S14 in Supporting Information S1), yielding ocean carbon uptake increases ranging from 0.29 to 0.58 mol C m^{-2} decade^{-1} μatm^{-1} (Figure 9d; Table S1 in Supporting Information S1). These results demonstrate that seasonal biases in carbon cycling representation, combined with changes in mean-state conditions, cause a divergence in winter $\Delta pCO_2^{sea\text{-}air}$ and sea-air CO_2 fluxes between models, leading to an increasing disagreement in the cumulative annual ocean carbon sink over time.

4. Conclusions

Systematic discrepancies in ocean carbon uptake between GOBMs pose an important challenge for the carbon cycle community to resolve, as these discrepancies can be interpreted as being reducible forms of uncertainty in climate model projections. In this study, we test the hypothesis that across-model discrepancies in decadal carbon uptake trends are partly sourced from systematic biases in seasonal carbon cycle representations. Using historical simulations from multiple GOBMs, we examine the mechanisms controlling the changes in surface ocean pCO_2 seasonal cycle amplitude and link across-model differences in C_{ant}-induced pCO_2 seasonality change to diverging trends in cumulative annual ocean carbon uptake. Consistent with Rodgers et al. (2023), we find that decadal increases in pCO_2 seasonal amplitudes are primarily driven by C_{ant} invasion (GOBM-ensemble global mean $\pm 1\sigma$ $= +5.9 \pm 0.6$ μatm), with smaller contributions from changes in climate state ($+0.7 \pm 0.5$ μatm; Figure 5). Within each model, C_{ant}-driven amplifications of seasonal pCO_2 cycles are primarily caused by an enhanced sensitivity of pCO_2 to seasonal thermal, biological, and physical processes via rising ocean carbon content and buffering capacity declines. In contrast, climate-driven alterations in seasonal pCO_2 amplitudes are mainly due to alterations in seasonal SST and DIC variability. In some models, climate-driven changes can locally outweigh the C_{ant}-induced amplification in equatorial and high latitude areas, yielding regional net declines in pCO_2 seasonal amplitudes.

Our analysis reveals how structural biases in SST and DIC seasonality representations systematically influence the across-model differences in C_{ant}-driven amplifications of thermal and biophysical pCO_2 seasonal cycles. We identify a direct link between a model's initial 1980–1984 seasonal amplitude of SST and DIC and the magnitude of thermal and biophysical $p\mathrm{CO}_2$ amplitude changes by 2014–2018, particularly when the $\mathrm{C}_{\mathrm{ant}}$ signal is not obscured by changes in the climate state (Figure 6). Models biased toward larger seasonal cycle amplitudes of SST or DIC simulate a proportionally larger $\mathrm{C}_{\mathrm{ant}}$-induced increase in thermal or biophysical $p\mathrm{CO}_2$ seasonal amplitudes, translating to an increasing divergence between models over time. Furthermore, as these models are systematically biased toward too-weak DIC seasonality (Rodgers et al., 2023), they exhibit an overemphasis of temperature-driven $p\mathrm{CO}_2$ seasonality globally and substantial inter-model disagreement in seasonal driver dominance in equatorial and high-latitude regions (Figure 7). Thus, the growing disagreement in $\mathrm{C}_{\mathrm{ant}}$-driven $p\mathrm{CO}_2$ amplitude change between models arises from differences in both the magnitude of initial surface $p\mathrm{CO}_2$ amplitudes and the spatial pattern of seasonal driver dominance, due to differences in mean-state SST and DIC seasonality. We therefore expect that diverging seasonal $p\mathrm{CO}_2$ amplification trends between GOBMs will become increasingly more pronounced over time in their current configurations, as $\mathrm{C}_{\mathrm{ant}}$ invasion will remain as the dominant anthropogenic signal under sustained fossil fuel emissions.

The growing across-model spread in $\mathrm{C}_{\mathrm{ant}}$-induced $p\mathrm{CO}_2$ amplification directly translates to diverging decadal trends in the cumulative annual ocean carbon sink between 1980 and 2018 (Figure 9). This trend divergence is primarily caused by increasing disagreements in the wintertime sea-air $p\mathrm{CO}_2$ disequilibrium, which is disproportionately enhanced by strong winter winds. As winter is the dominant season for sea-air CO_2 fluxes, the diverging wintertime sink strengths directly contribute to a progressively inconsistent annual ocean carbon uptake. An important implication of this key finding is that we have identified a clear link between the seasonal carbon cycle and the annual mean-state for sea-air CO_2 fluxes within individual GOBMs (Figure S12 in Supporting Information S1). The use of multiple GOBMs was instrumental in establishing and understanding this relationship. We highlight that these timescales are not independent, and thus, persistent seasonal discrepancies in the ocean carbon cycle should be expected to exacerbate longer-term annual mean-state trend discrepancies over time.

In closing, this study demonstrates that the seasonal carbon cycle provides a valuable lens for assessing the utility of GOBMs in simulating ocean carbon uptake trends. For GOBMs to be appropriately used for carbon cycle synthesis efforts, sources of uncertainty (e.g., model structural uncertainty, forcing uncertainty, spin-up uncertainty) should be randomly distributed about the state of the real system. For the case of seasonal variability in surface DIC concentrations, state-of-the-art observational products are consistent in pointing toward a systematic bias in the model seasonal amplitude (Rodgers et al., 2023), providing the motivation for the investigation presented here. The existence of such a systematic bias complicates the conventional approach of interpreting a multi-model mean as being a "best-estimate" of the trend in CO_2 uptake by the ocean. Although it is our intention that our results should be of benefit to interpretations of model-data discrepancies in future synthesis efforts, it simultaneously clarifies the central importance of developing improved mechanistic understanding of the seasonal cycle of sea surface DIC concentrations as a basis for improving projections skill for future interactions between the carbon cycle and the other components of the climate system.

Conflict of Interest

The authors declare no conflicts of interest relevant to this study.

Availability Statement

All model data can be found in the RECCAP2 data repository at https://doi.org/10.5281/zenodo.7990823 (Müller, 2023).

Acknowledgments
We thank the research groups contributing to the RECCAP2 and Global Carbon Project synthesis efforts. We also thank Brendan R. Carter for valuable feedback during manuscript drafting as well as two anonymous reviewers and the editor for their constructive comments that greatly helped us improve the scope and clarity of this manuscript. M.C.A was supported by University of California Santa Cruz and the ARCS Foundation of Northern California. A.J.F was supported by NOAA Pacific Marine Environmental Laboratory. The contribution of K.B.R. was provided through the World Premier International Research Center Initiative (WPI), funded by the Ministry of Education, Culture, Sports, Science and Technology (MEXT), Japan. This is PMEL contribution #5763.

References

Aumont, O., Ethé, C., Tagliabue, A., Bopp, L., & Gehlen, M. (2015). PISCES-v2: An ocean biogeochemical model for carbon and ecosystem studies. *Geoscientific Model Development*, *8*(8), 2465–2513. https://doi.org/10.5194/gmd-8-2465-2015

Berthet, S., Séférian, R., Bricaud, C., Chevallier, M., Voldoire, A., & Ethé, C. (2019). Evaluation of an online grid-coarsening algorithm in a global eddy-admitting ocean biogeochemical model. *Journal of Advances in Modeling Earth Systems*, *11*(6), 1759–1783. https://doi.org/10.1029/2019MS001644

Broecker, W. S., Takahashi, T., Simpson, H. J., & Peng, T.-H. (1979). Fate of fossil fuel carbon dioxide and the global carbon budget. *Science*, *206*(4417), 409–418. https://doi.org/10.1126/science.206.4417.409

Bushinsky, S. M., Landschützer, P., Rödenbeck, C., Gray, A. R., Baker, D., Mazloff, M. R., et al. (2019). Reassessing southern ocean air-sea CO_2 flux estimates with the addition of biogeochemical float observations. *Global Biogeochemical Cycles*, *33*(11), 1370–1388. https://doi.org/10.1029/2019GB006176

Chien, C.-T., Durgadoo, J. V., Ehlert, D., Frenger, I., Keller, D. P., Koeve, W., et al. (2022). FOCI-MOPS v1—Integration of marine biogeochemistry within the Flexible Ocean and Climate Infrastructure version 1 (FOCI 1) Earth system model. *Geoscientific Model Development*, *15*(15), 5987–6024. https://doi.org/10.5194/gmd-15-5987-2022

DeVries, T., Yamamoto, K., Wanninkhof, R., Gruber, N., Hauck, J., Müller, J. D., et al. (2023). Magnitude, trends, and variability of the global ocean carbon sink from 1985 to 2018. *Global Biogeochemical Cycles*, *37*(10), e2023GB007780. https://doi.org/10.1029/2023GB007780

Dickson, A. G., Wesolowski, D. J., Palmer, D. A., & Mesmer, R. E. (1990). Dissociation constant of bisulfate ion in aqueous sodium chloride solutions to 250°C. *Journal of Physical Chemistry*, *94*(20), 7978–7985. https://doi.org/10.1021/j100383a042

Doney, S. C., Lima, I., Feely, R. A., Glover, D. M., Lindsay, K., Mahowald, N., et al. (2009). Mechanisms governing interannual variability in upper-ocean inorganic carbon system and air–sea CO_2 fluxes: Physical climate and atmospheric dust. *Deep Sea Research Part II: Topical Studies in Oceanography*, *56*(8), 640–655. https://doi.org/10.1016/j.dsr2.2008.12.006

Döscher, R., Acosta, M., Alessandri, A., Anthoni, P., Arsouze, T., Bergman, T., et al. (2022). The EC-Earth3 Earth system model for the Coupled Model Intercomparison Project 6. *Geoscientific Model Development*, *15*(7), 2973–3020. https://doi.org/10.5194/gmd-15-2973-2022

Egleston, E. S., Sabine, C. L., & Morel, F. M. M. (2010). Revelle revisited: Buffer factors that quantify the response of ocean chemistry to changes in DIC and alkalinity. *Global Biogeochemical Cycles*, *24*(1). https://doi.org/10.1029/2008GB003407

Fassbender, A. J., Rodgers, K. B., Palevsky, H. I., & Sabine, C. L. (2018). Seasonal asymmetry in the evolution of surface ocean pCO_2 and pH thermodynamic drivers and the influence on sea-air CO_2 flux. *Global Biogeochemical Cycles*, *32*(10), 1476–1497. https://doi.org/10.1029/2017GB005855

Fassbender, A. J., Sabine, C. L., & Palevsky, H. I. (2017). Nonuniform ocean acidification and attenuation of the ocean carbon sink. *Geophysical Research Letters*, *44*(16), 8404–8413. https://doi.org/10.1002/2017GL074389

Fassbender, A. J., Schlunegger, S., Rodgers, K. B., & Dunne, J. P. (2022). Quantifying the role of seasonality in the marine carbon cycle feedback: An ESM2M case study. *Global Biogeochemical Cycles*, *36*(6), e2021GB007018. https://doi.org/10.1029/2021gb007018

Fay, A. R., & McKinley, G. A. (2021). Observed regional fluxes to constrain modeled estimates of the ocean carbon sink. *Geophysical Research Letters*, *48*(20), e2021GL095325. https://doi.org/10.1029/2021GL095325

Friedlingstein, P., O'Sullivan, M., Jones, M. W., Andrew, R. M., Hauck, J., Landschützer, P., et al. (2024). Global Carbon Budget 2024. *Earth System Science Data Discussions*, 1–133. https://doi.org/10.5194/essd-2024-519

Gallego, M., Timmermann, A., Friedrich, T., & Zeebe, R. E. (2018). Drivers of future seasonal cycle changes in oceanic pCO_2. *Biogeosciences*, *15*(17), 5315–5327. https://doi.org/10.5194/bg-15-5315-2018

Gloege, L., McKinley, G. A., Landschützer, P., Fay, A. R., Frölicher, T. L., Fyfe, J. C., et al. (2021). Quantifying errors in observationally based estimates of ocean carbon sink variability. *Global Biogeochemical Cycles*, *35*(4), e2020GB006788. https://doi.org/10.1029/2020GB006788

Gorgues, T., Aumont, O., & Rodgers, K. B. (2010). A mechanistic account of increasing seasonal variations in the rate of ocean uptake of anthropogenic carbon. *Biogeosciences*, *7*(8), 2581–2589. https://doi.org/10.5194/bg-7-2581-2010

Goris, N., Tjiputra, J. F., Olsen, A., Schwinger, J., Lauvset, S. K., & Jeansson, E. (2018). Constraining projection-based estimates of the future North Atlantic carbon uptake. *Journal of Climate*, *31*(10), 3959–3978. https://doi.org/10.1175/JCLI-D-17-0564.1

Gregor, L., Lebehot, A. D., Kok, S., & Scheel Monteiro, P. M. (2019). A comparative assessment of the uncertainties of global surface ocean CO_2 estimates using a machine-learning ensemble (CSIR-ML6 version 2019a)—Have we hit the wall? *Geoscientific Model Development*, *12*(12), 5113–5136. https://doi.org/10.5194/gmd-12-5113-2019

Gruber, N., Clement, D., Carter, B. R., Feely, R. A., van Heuven, S., Hoppema, M., et al. (2019). The oceanic sink for anthropogenic CO_2 from 1994 to 2007. *Science*, *363*(6432), 1193–1199. https://doi.org/10.1126/science.aau5153

Hauck, Nissen, C., Landschützer, P., Rödenbeck, C., Bushinsky, S., & Olsen, A. (2023). Sparse observations induce large biases in estimates of the global ocean CO_2 sink: An ocean model subsampling experiment. *Philosophical Transactions of the Royal Society A: Mathematical, Physical and Engineering Sciences*, *381*(2249), 20220063. https://doi.org/10.1098/rsta.2022.0063

Hauck, & Völker, C. (2015). Rising atmospheric CO_2 leads to large impact of biology on Southern Ocean CO_2 uptake via changes of the Revelle factor. *Geophysical Research Letters*, *42*(5), 1459–1464. https://doi.org/10.1002/2015GL063070

Hauck, Zeising, M., Le Quéré, C., Gruber, N., Bakker, D. C. E., Bopp, L., et al. (2020). Consistency and challenges in the ocean carbon sink estimate for the global carbon budget. *Frontiers in Marine Science*, *7*. https://doi.org/10.3389/fmars.2020.571720

Kalnay, E., Kanamitsu, M., Kistler, R., Collins, W., Deaven, D., Gandin, L., et al. (1996). The NCEP/NCAR 40-year reanalysis project. *Bulletin of the American Meteorological Society*, *77*(3), 437–471. https://doi.org/10.1175/1520-0477(1996)077<0437:TNYRP>2.0.CO;2

Kessler, A., & Tjiputra, J. (2016). The Southern Ocean as a constraint to reduce uncertainty in future ocean carbon sinks. *Earth System Dynamics*, *7*(2), 295–312. https://doi.org/10.5194/esd-7-295-2016

Khatiwala, S., Tanhua, T., Mikaloff Fletcher, S., Gerber, M., Doney, S. C., Graven, H. D., et al. (2013). Global ocean storage of anthropogenic carbon. *Biogeosciences*, *10*(4), 2169–2191. https://doi.org/10.5194/bg-10-2169-2013

Kobayashi, S., Ota, Y., Harada, Y., Ebita, A., Moriya, M., Onoda, H., et al. (2015). The JRA-55 reanalysis: General specifications and basic characteristics. *Journal of the Meteorological Society of Japan. Ser. II*, *93*(1), 5–48. https://doi.org/10.2151/jmsj.2015-001

Kriest, I., & Oschlies, A. (2015). MOPS-1.0: Towards a model for the regulation of the global oceanic nitrogen budget by marine biogeochemical processes. *Geoscientific Model Development*, *8*(9), 2929–2957. https://doi.org/10.5194/gmd-8-2929-2015

Kwiatkowski, L., & Orr, J. C. (2018). Diverging seasonal extremes for ocean acidification during the twenty-first century. *Nature Climate Change*, *8*(2), 141–145. https://doi.org/10.1038/s41558-017-0054-0

Landschützer, P., Gruber, N., Bakker, D. C. E., Stemmler, I., & Six, K. D. (2018). Strengthening seasonal marine CO_2 variations due to increasing atmospheric CO_2. *Nature Climate Change*, *8*(2), 146–150. https://doi.org/10.1038/s41558-017-0057-x

Large, W. G., & Yeager, S. G. (2009). The global climatology of an interannually varying air–sea flux data set. *Climate Dynamics*, *33*(2), 341–364. https://doi.org/10.1007/s00382-008-0441-3

Lee, K., Kim, T.-W., Byrne, R. H., Millero, F. J., Feely, R. A., & Liu, Y.-M. (2010). The universal ratio of boron to chlorinity for the North Pacific and North Atlantic oceans. *Geochimica et Cosmochimica Acta*, *74*(6), 1801–1811. https://doi.org/10.1016/j.gca.2009.12.027

Lewis, E., & Wallace, D. W. R. (1998). *CO2SYS—Program developed for the CO_2 system calculations. ORNL/CDIAC-105*. Carbon Dioxide Information Analysis Center, Oak Ridge National Laboratory, U.S. Department of Energy. Publication no. 4735.

Lindsay, K., Bonan, G. B., Doney, S. C., Hoffman, F. M., Lawrence, D. M., Long, M. C., et al. (2014). Preindustrial-control and twentieth-century Carbon Cycle Experiments with the Earth System Model CESM1(BGC). *Journal of Climate*, *27*(24), 8981–9005. https://doi.org/10.1175/JCLI-D-12-00565.1

Lueker, T. J., Dickson, A. G., & Keeling, C. D. (2000). Ocean pCO_2 calculated from dissolved inorganic carbon, alkalinity, and equations for K1 and K2: Validation based on laboratory measurements of CO_2 in gas and seawater at equilibrium. *Marine Chemistry*, *70*(1–3), 105–119. https://doi.org/10.1016/S0304-4203(00)00022-0

Mayot, N., Buitenhuis, E. T., Wright, R. M., Hauck, J., Bakker, D. C. E., & Le Quéré, C. (2024). Constraining the trend in the ocean CO_2 sink during 2000–2022. *Nature Communications*, *15*(1), 8429. https://doi.org/10.1038/s41467-024-52641-7

Middelburg, J. J., Soetaert, K., & Hagens, M. (2020). Ocean alkalinity, buffering and biogeochemical processes. *Reviews of Geophysics*, *58*(3), e2019RG000681. https://doi.org/10.1029/2019RG000681

Mongwe, N. P., Vichi, M., & Monteiro, P. M. S. (2018). The seasonal cycle of pCO_2 and CO_2 fluxes in the Southern Ocean: Diagnosing anomalies in CMIP5 Earth system models. *Biogeosciences*, *15*(9), 2851–2872. https://doi.org/10.5194/bg-15-2851-2018

Müller, J. D. (2023). RECCAP2-ocean data collection. https://doi.org/10.5281/zenodo.7990823

Müller, J. D., Gruber, N., Carter, B., Feely, R., Ishii, M., Lange, N., et al. (2023). Decadal trends in the oceanic storage of anthropogenic carbon from 1994 to 2014. *AGU Advances*, *4*(4), e2023AV000875. https://doi.org/10.1029/2023AV000875

Nevison, C. D., Manizza, M., Keeling, R. F., Stephens, B. B., Bent, J. D., Dunne, J., et al. (2016). Evaluating CMIP5 ocean biogeochemistry and Southern Ocean carbon uptake using atmospheric potential oxygen: Present-day performance and future projection. *Geophysical Research Letters*, *43*(5), 2077–2085. https://doi.org/10.1002/2015GL067584

Perez, F. F., & Fraga, F. (1987). Association constant of fluoride and hydrogen ions in seawater. *Marine Chemistry*, *21*(2), 161–168. https://doi.org/10.1016/0304-4203(87)90036-3

Revelle, R., & Suess, H. E. (1957). Carbon dioxide exchange between atmosphere and ocean and the question of an increase of atmospheric CO_2 during the past decades. *Tellus*, *9*(1), 18–27. https://doi.org/10.1111/j.2153-3490.1957.tb01849.x

Riebesell, U., Kortzinger, A., & Oschlies, A. (2009). Sensitivities of marine carbon fluxes to ocean change. *Proceedings of the National Academy of Sciences*, *106*(49), 20602–20609. https://doi.org/10.1073/pnas.0813291106

Rödenbeck, C., Bakker, D. C. E., Gruber, N., Iida, Y., Jacobson, A. R., Jones, S., et al. (2015). Data-based estimates of the ocean carbon sink variability - First results of the Surface Ocean pCO_2 Mapping intercomparison (SOCOM). *Biogeosciences*, *12*(23), 7251–7278. https://doi.org/10.5194/bg-12-7251-2015

Rodgers, K. B., Sarmiento, J. L., Aumont, O., Crevoisier, C., de Boyer Montégut, C., & Metzl, N. (2008). A wintertime uptake window for anthropogenic CO_2 in the North Pacific. *Global Biogeochemical Cycles*, *22*(2). https://doi.org/10.1029/2006GB002920

Rodgers, K. B., Schlunegger, S., Slater, R. D., Ishii, M., Frölicher, T. L., Toyama, K., et al. (2020). Reemergence of anthropogenic carbon into the ocean's mixed layer strongly amplifies transient climate sensitivity. *Geophysical Research Letters*, *47*(18). https://doi.org/10.1029/2020GL089275

Rodgers, Schwinger, J., Fassbender, A. J., Landschützer, P., Yamaguchi, R., Frenzel, H., et al. (2023). Seasonal variability of the surface ocean carbon cycle: A synthesis. *Global Biogeochemical Cycles*, *37*(9), e2023GB007798. https://doi.org/10.1029/2023GB007798

Rustogi, P., Landschützer, P., Brune, S., & Baehr, J. (2023). The impact of seasonality on the annual air-sea carbon flux and its interannual variability. *Npj Climate and Atmospheric Science*, *6*(1). https://doi.org/10.1038/s41612-023-00378-3

Schwinger, J., Goris, N., Tjiputra, J. F., Kriest, I., Bentsen, M., Bethke, I., et al. (2016). Evaluation of NorESM-OC (versions 1 and 1.2), the ocean carbon-cycle stand-alone configuration of the Norwegian Earth System Model (NorESM1). *Geoscientific Model Development*, *9*(8), 2589–2622. https://doi.org/10.5194/gmd-9-2589-2016

Séférian, R., Delire, C., Decharme, B., Voldoire, A., Salas y Melia, D., Chevallier, M., et al. (2016). Development and evaluation of CNRM Earth system model—CNRM-ESM1. *Geoscientific Model Development*, *9*(4), 1423–1453. https://doi.org/10.5194/gmd-9-1423-2016

Séférian, R., Gehlen, M., Bopp, L., Resplandy, L., Orr, J. C., Marti, O., et al. (2016). Inconsistent strategies to spin up models in CMIP5: Implications for ocean biogeochemical model performance assessment. *Geoscientific Model Development*, *9*(5), 1827–1851. https://doi.org/10.5194/gmd-9-1827-2016

Séférian, R., Nabat, P., Michou, M., Saint-Martin, D., Voldoire, A., Colin, J., et al. (2019). Evaluation of CNRM Earth system model, CNRM-ESM2-1: Role of Earth system processes in present-day and future climate. *Journal of Advances in Modeling Earth Systems*, *11*(12), 4182–4227. https://doi.org/10.1029/2019MS001791

Sharp, J. D., Pierrot, D., Humphreys, M. P., Epitalon, J.-M., Orr, J. C., Lewis, E. R., & Wallace, D. W. R. (2020). *CO2SYSv3 for MATLAB (Version v3.0)*. Zenodo. https://doi.org/10.5281/zenodo.3950563

Takahashi, T., Broecker, W. S., Werner, S. R., & Bainbridge, A. E. (1980). Carbonate chemistry of the surface waters of the worlds oceans. In K. S. Edward, D. Goldberg, & Y. Horibe (Eds.), *Isotope Marine Chemistry* (pp. 292–326).

Takahashi, T., Olafsson, J., Goddard, J. G., Chipman, D. W., & Sutherland, S. C. (1993). Seasonal variation of CO_2 and nutrients in the high-latitude surface oceans: A comparative study. *Global Biogeochemical Cycles*, *7*(4), 843–878. https://doi.org/10.1029/93GB02263

Takahashi, T., Sutherland, S. C., Sweeney, C., Poisson, A., Metzl, N., Tilbrook, B., et al. (2002). Global sea–air CO_2 flux based on climatological surface ocean pCO_2, and seasonal biological and temperature effects. *Deep Sea Research Part II: Topical Studies in Oceanography*, *49*(9–10), 1601–1622. https://doi.org/10.1016/S0967-0645(02)00003-6

Terhaar, J., Frölicher, T. L., & Joos, F. (2022). Observation-constrained estimates of the global ocean carbon sink from Earth system models. *Biogeosciences*, *19*(18), 4431–4457. https://doi.org/10.5194/bg-19-4431-2022

Terhaar, J., Goris, N., Müller, J. D., DeVries, T., Gruber, N., Hauck, J., et al. (2024). Assessment of global ocean biogeochemistry models for ocean carbon sink estimates in RECCAP2 and recommendations for future studies. *Journal of Advances in Modeling Earth Systems*, *16*(3), e2023MS003840. https://doi.org/10.1029/2023MS003840

Thyng, K. M., Greene, C. A., Hetland, R. D., Zimmerle, H. M., & DiMarco, S. F. (2016). True colors of oceanography: Guidelines for effective and accurate colormap selection. *Oceanography*, *29*(3), 9–13. https://doi.org/10.5670/oceanog.2016.66

Toyama, K., Rodgers, K. B., Blanke, B., Iudicone, D., Ishii, M., Aumont, O., & Sarmiento, J. L. (2017). Large reemergence of anthropogenic carbon into the ocean's surface mixed layer sustained by the ocean's overturning. *Circulation*, *30*(21), 8615–8631. https://doi.org/10.1175/JCLI-D-16-0725.1

van Heuven, S., Pierrot, D., Rae, J. W. B., Lewis, E., & Wallace, D. W. R. (2011). *MATLAB program developed for CO_2 system calculations. ORNL/CDIAC-105b*. Carbon Dioxide Information Analysis Center, Oak Ridge National Laboratory, U.S. Department of Energy. https://doi.org/10.3334/CDIAC/otg.CO2SYS_MATLAB_v1.1

Wanninkhof, R. (2014). Relationship between wind speed and gas exchange over the ocean revisited. *Limnology and Oceanography: Methods*, *12*(6), 351–362. https://doi.org/10.4319/lom.2014.12.351

Wanninkhof, R., Park, G.-H., Takahashi, T., Sweeney, C., Feely, R., Nojiri, Y., et al. (2013). Global ocean carbon uptake: Magnitude, variability and trends. *Biogeosciences*, *10*(3), 1983–2000. https://doi.org/10.5194/bg-10-1983-2013

Yang, S., & Gruber, N. (2016). The anthropogenic perturbation of the marine nitrogen cycle by atmospheric deposition: Nitrogen cycle feedbacks and the 15N Haber-Bosch effect. *Global Biogeochemical Cycles*, *30*(10), 1418–1440. https://doi.org/10.1002/2016GB005421